Available online at www.sciencedirect.com

ScienceDirect

Geochimica et Cosmochimica Acta 239 (2018) 235–254

Geochimica et Cosmochimica Acta

www.elsevier.com/locate/gca

The behaviour of ferric iron during partial melting of peridotite

Fanny Sorbadere [a,1], Vera Laurenz [a,*], Daniel J. Frost [a], Michelle Wenz [a,2], Anja Rosenthal [a,3], Catherine McCammon [a], Camille Rivard [b,4]

[a] *Bayerisches Geoinstitut, University of Bayreuth, Bayreuth D-95440, Germany*
[b] *ESRF-The European Synchrotron, 38000 Grenoble, France*

Received 30 March 2017; accepted in revised form 10 July 2018; available online 18 July 2018

Abstract

In order to better understand the behaviour of Fe^{3+} during partial melting of a mid-ocean-ridge-basalt (MORB) mantle source, we performed partial melting experiments of a spinel peridotite at 1.5 GPa, between 1320 and 1450 °C, and over a range of oxygen fugacities (fO_2) varying from FMQ-3.5 to FMQ+6 (log-units relative to FMQ = Fayalite-Magnetite-Quartz oxygen buffer). Changes in fO_2 were achieved using different capsule materials and by varying the oxidation state of the starting material. Fe^{3+} contents of spinels and glasses were examined using Fe *K*-edge X-ray Absorption Near Edge Structure (XANES) spectroscopy in full-field mode. Our results show that this method allows $Fe^{3+}/\Sigma Fe$ measurements to be made of spinels in our experimental charges but is not suitable for quantifying $Fe^{3+}/\Sigma Fe$ of glasses, particularly at relatively low fO_2 where melt Fe_2O_3 contents are small. We therefore employed several methods ($Fe^{3+}/\Sigma Fe$ ratios of spinels measured by XANES and calculated by stoichiometry, and Fe-alloy sliding redox sensors) to assess the fO_2 of the samples. These were then used to calculate the $Fe^{3+}/\Sigma Fe$ ratios of glasses using published models, which were further constrained by Mössbauer spectroscopy measurements on an additional set of partial melting experiments.

For a particular initial redox state, the $Fe^{3+}/\Sigma Fe$ ratio in melts remains approximately constant with partial melting degree. This is explained by a slight decrease of the bulk partition coefficient of Fe_2O_3 ($D_{Fe_2O_3}^{peridotite-melt}$) as the degree of partial melting increases. The $Fe^{3+}/\Sigma Fe$ ratios of resulting melts are thus restricted to a relatively narrow range over large degrees of melting, as observed for global MORB glass analyses. This observation is also confirmed by pMELTS calculations employing different bulk $Fe^{3+}/\Sigma Fe$ ratios. We conclude that the Fe_2O_3 content in MORB can be accounted for through partial melting of a mantle source containing 0.1–0.5 wt% Fe_2O_3 and a bulk $D_{Fe_2O_3}^{peridotite-melt}$ ranging from 0.3 to 0.1.

1. INTRODUCTION

Mantle oxygen fugacity (fO_2) has wide-ranging implications for many Earth-system processes, such as those that established the composition of the atmosphere (Hirschmann, 2012) or in general any process dependent on transport properties of mantle rocks (Mackwell, 2008). Oxygen fugacities have been estimated for the mantle based on mineral oxybarometers (e.g., O'Neill and Wall, 1987; Ballhaus et al., 1991; Davis et al., 2017) and abundances and ratios of redox-sensitive trace elements in basalts and peridotites (e.g., Canil, 2002). Probably the most commonly

* Corresponding author.
E-mail address: vera.laurenz@uni-bayreuth.de (V. Laurenz).
[1] Present address: Creation Volcans, 2 rue Roger Varenne, 63500 Issoire, France.
[2] Present address: Department of Earth and Planetary Sciences, Northwestern University, Evanston, IL 60208, USA.
[3] Present address: Magmas and Volcanoes Laboratory, Clermont Auvergne University, CNRS, IRD, OPGC, 63000 Clermont-Ferrand, France.
[4] Present address: CEPIA, INRA, 44300 Nantes, France and Synchrotron SOLEIL, 91192 Gif-sur-Yvette, France.

https://doi.org/10.1016/j.gca.2018.07.019
0016-7037/

used proxy for the asthenosphere is the oxidation state of iron in primitive melts (Kasting et al., 1993; Lécuyer and Ricard, 1999; Gaillard et al., 2015; Gaetani; 2016), which has been proposed to be directly related to the fO_2 of their source region (Carmichael, 1991; Kress and Carmichael, 1991). Recently measured $Fe^{3+}/\Sigma Fe$ ratios determined for mid ocean ridge basalts (MORB) show a very narrow range in values, with standard deviations of only a few percent. Most likely as a result of different analytical techniques, the proposed global average $Fe^{3+}/\Sigma Fe$ ratios vary somewhat between studies, e.g. 0.12 ± 0.02 (Bézos and Humler, 2005) and 0.16 ± 0.01 (Cottrell and Kelley, 2011). Regardless of the technique employed, these studies imply fairly constant mantle oxygen fugacities close to the Fayalite-Magnetite-Quartz buffer (FMQ - O'Neill and Wall, 1987). Studies of other redox sensitive elements such as V and Cr, which have variable valence states and partition coefficients as a function of fO_2 (Canil et al., 2006; Mallmann and O'Neill, 2009, 2013), also seem to imply that mantle melting occurs over a relatively small range of fO_2. Since Fe^{3+} behaves incompatibly during partial melting with a bulk mineral-melt partition coefficient ($D^{peridotite-melt}_{Fe_2O_3}$) of ~0.1 (Holloway and Burnham, 1972; Canil et al., 1994; Mallmann and O'Neill, 2009), MORB $Fe^{3+}/\Sigma Fe$ ratios are expected to be essentially controlled by magmatic processes of partial melting and fractional crystallisation, similar to other incompatible elements. Weak correlations between $Fe^{3+}/\Sigma Fe$ ratios and indices of low pressure fractional crystallization have been recognized in some MORB measurements (Cottrell and Kelley, 2011), but the clear lack of correlations in many individual magmatic suites has led some researchers to conclude that differentiation processes may vary potentially even between ridge segments, in terms of whether they are open or closed to oxygen (Bézos and Humler, 2005). Correlations that would be expected between $Fe^{3+}/\Sigma Fe$ ratios and melt-fraction related parameters, such as $Na_2O_{(8)}$ (i.e. Na_2O concentration corrected for fractional crystallization to 8 wt% MgO - Klein and Langmuir, 1987) have not been found in MORB (Bézos and Humler, 2005; Cottrell and Kelley, 2011). Put simply, while indices for the degree of partial melting vary strongly between basalt samples, $Fe^{3+}/\Sigma Fe$ ratios do not.

Several hypotheses have been suggested to explain this paradox: the fO_2 might be buffered by chemical reactions during partial melting of the mantle. Phases such as graphite (Kadik, 1997; Holloway, 1998; Bézos and Humler, 2005), or sulfide (Cottrell and Kelley, 2011) may act to reduce ferric to ferrous iron so that the $Fe^{3+}/\Sigma Fe$ ratio of MORB is maintained at a constant value, regardless of the melting degree. Another possibility involves variations of bulk $D^{peridotite-melt}_{Fe_2O_3}$ as a function of the degree of peridotite melting or oxygen fugacity (Cottrell and Kelley 2011; Gaetani, 2016). Being an incompatible element, Fe^{3+} is expected to show a positive correlation with other incompatible elements such as TiO_2 or $Na_2O_{(8)}$ at variable degrees of partial melting (e.g. Bézos and Humler, 2005). This would have to be offset by a process that would make Fe^{3+} more incompatible at higher degrees of melting. Nevertheless, because of the lack of experimental data on the behaviour of Fe^{3+} during partial melting of a MORB-mantle source region, these hypotheses are based essentially on assumptions and geochemical modelling.

In this study, the effects of temperature and fO_2 on the $Fe^{3+}/\Sigma Fe$ ratio of peridotite melts and on mineral-melt Fe^{3+} partition coefficients have been determined experimentally using the results of partial melting experiments on a MORB-mantle source composition. The experiments were performed at 1.5 GPa and temperatures between 1310 and 1450 °C, which are suitable conditions for MORB genesis (e.g. Green and Falloon, 1998, 2005; Green et al., 2001; Lee et al., 2009). Oxygen fugacity was varied from FMQ-3.5 to FMQ+6. $Fe^{3+}/\Sigma Fe$ ratios of melts and spinels were measured using Fe *K*-edge X-ray Absorption Near Edge Structure (XANES) spectroscopy analyses, conducted using a full-field imaging setup, which provides superior statistics on spinel measurements. In order to determine precise fO_2 values and test the consistency of our measurements, we compare our XANES data with different thermodynamic models. The results are applied to understanding the behaviour of ferric iron during partial melting of the mantle and to explaining the constant $Fe^{3+}/\Sigma Fe$ ratio observed for MORB.

2. EXPERIMENTAL PROCEDURE

2.1. Starting materials

Due to its proposed similarity to the source rock of primitive MORB melts, we used a synthetic peridotite composition called MORB-pyrolite "MPY-90" as a starting composition (Falloon and Green, 1987). The initial starting powder was obtained by mixing analytical grade oxides and carbonates. The mixes were decarbonated at 800 °C in air and subsequently reduced for 24 h at 1100 °C in a CO/CO_2 atmosphere under different fO_2 conditions. Four different starting materials were prepared, ranging from reducing conditions of FMQ-2 (i.e. 2 log-units below the FMQ-buffer), intermediate conditions (FMQ-1 and FMQ), to highly oxidizing conditions that were equilibrated in air (Table 1). Some of the material reduced at FMQ-2 and FMQ was additionally mixed with 3% of IrO_2 in order to determine the fO_2 of the run products (Woodland and O' Neill , 1997; Stagno and Frost, 2010).

2.2. High pressure experiments

Partial melting experiments were performed in a ½ inch piston-cylinder apparatus at 1.5 GPa between 1310 and 1450 °C, i.e. suitable *P-T* conditions for MORB generation (e.g. Lee et al., 2009). Talc-Pyrex piston cylinder assemblies were employed with tapered graphite furnaces. Crushable Al_2O_3 spacers and capsule sleeves were used inside the furnace. Temperature was measured using a type D ($W_{75}Re_{25}$-$W_{97}Re_3$) thermocouple and maintained within 1° of the setpoint using a Eurotherm controller. To ensure chemical and textural equilibrium, run durations varied from 24 to 48 h, depending on temperature.

Table 1
Overview of piston-cylinder experiments at 1.5 GPa.

Sample	capsule material	ΔFMQ starting material	Run time (h)	T (°C)	phases present
Graph-1320	graphite-lined Pt	−2	49	1320	gl,ol,opx,cpx,spi
Graph-1370	graphite-lined Pt	−2	40	1370	gl,ol,opx,cpx,spi
Graph-1400	graphite-lined Pt	−2	24	1400	gl,ol,opx,cpx,spi
Graph-1450	graphite-lined Pt	−2	24	1450	gl,ol,opx,cpx,spi
Re1-1320	Re-lined Pt	−2	50	1320	gl,ol,opx,cpx,spi
Re1-1340	Re-lined Pt	−2	48	1340	gl,ol,opx,cpx,spi
Re1-1370	Re-lined Pt	−2	30	1370	gl,ol,opx,cpx,spi
Re1-1400	Re-lined Pt	−2	24	1400	gl,ol,opx,spi,
Re1-1440	Re-lined Pt	−2	24	1440	gl,ol,opx,spi,
Re2-1320	Re-lined Pt	0	50	1320	gl,ol,opx,cpx,spi
Re2-1370	Re-lined Pt	0	30	1370	gl,ol,opx,cpx,spi
Re2-1400	Re-lined Pt	0	24	1400	gl,ol,opx,spi,
Re2-1440	Re-lined Pt	0	24	1440	gl,ol,spi,
AuPd1-1310	$Au_{80}Pd_{20}$	−1	48	1310	gl,ol,opx,cpx,spi
AuPd1-1330	$Au_{80}Pd_{20}$	−1	48	1330	gl,ol,opx,cpx,spi
AuPd1-1360	$Au_{80}Pd_{20}$	−1	45	1360	gl,ol,opx,cpx,spi
AuPd1-1390	$Au_{80}Pd_{20}$	−1	24	1390	gl,ol,opx,spi,
AuPd2-1320	$Au_{80}Pd_{20}$	Air	48	1320	gl,ol,opx,cpx,spi
AuPd2-1330	$Au_{80}Pd_{20}$	Air	48	1330	gl,ol,opx,cpx,spi
AuPd2-1350	$Au_{80}Pd_{20}$	Air	30	1350	gl,ol,opx,cpx,spi
AuPd2-1370	$Au_{80}Pd_{20}$	Air	24	1370	gl,ol,opx,spi,

gl = glass, ol = olivine, opx = orthopyroxene, cpx = clinopyroxene, spi = spinel.

In order to maintain distinct fO_2 conditions during the experiments, different combinations of capsule types and starting materials were employed (Fig. 1, Table 1). Experiments with the prefix "Graph" were performed using graphite-lined Pt-capsules and samples of MPY-90 starting material that had been initially reduced at FMQ-2. Experiments with the prefix "Re" employed outer capsules of platinum lined with an inner Re-foil encapsulating the entire MPY-90 sample powder, which was either reduced at FMQ-2 for experiments "Re1", or at FMQ for experiments with the prefix "Re2". "AuPd1" experiments were performed using $Au_{80}Pd_{20}$ capsules with a MPY-90 starting material reduced at FMQ-1, while for "AuPd2" experiments a highly oxidized MPY-90 starting material (i.e., equilibrated in air) was used. The fO_2 therefore increased from the most reduced "Graph" experiments through the intermediate "Re1", "AuPd1" and "Re2" experiments, to the most oxidized "AuPd2" experiments. To minimize the absorption of water, all powders and assemblies were stored under vacuum in an oven at 100 °C. Starting materials were heated at 250 °C for one day before each experiment and Al_2O_3 pieces were dried for 1 h at 1000 °C. Finally, the capsule was fired for 10 s using a blowtorch immediately before welding.

In order to generate large enough melt pools for analysis of the silicate melt compositions in equilibrium with residual mineral phases, different melt extraction techniques were used, depending on the capsule type. For "Graph" experiments, the micro-dike technique developed by Laporte et al. (2004) was used, whereby melt is trapped within cracks formed in the graphite sample chamber. For "Re" experiments, additional layers of Re foil were placed at the bottom and the top of the capsule and liquid was trapped between these layers. In "AuPd" experiments, the liquid was trapped within folds of the capsule that were formed by squeezing it before welding. In experiments

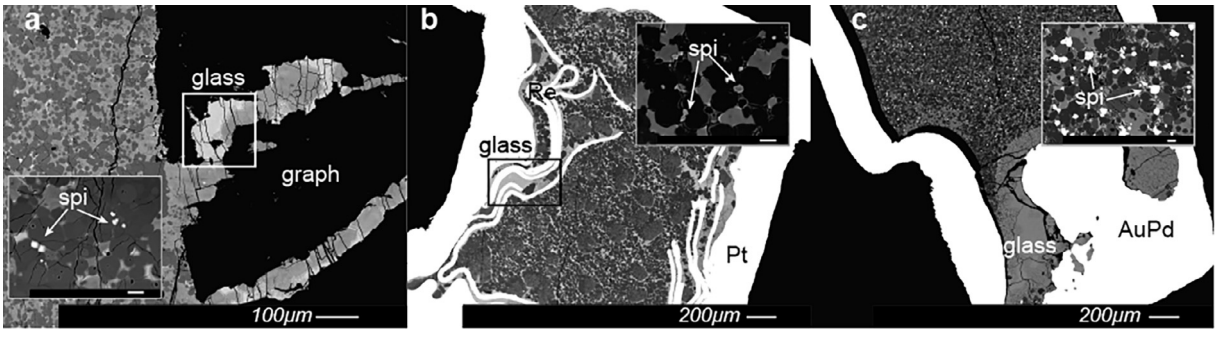

Fig. 1. Back scattered electron images of representative partial melting experiments using (a) platinum (Pt) capsules containing a graphite (graph) sleeve, (b) platinum capsules with a rhenium (Re) sleeve and (c) gold/palladium (AuPd) capsule. Scale bars of the inset pictures showing spinels (spi) are 10 µm. The separation of melt (glass) into cracks and folds in each capsule is shown.

employing each technique the liquids remained in equilibrium with neighbouring mineral phases because they were in physical contact with each other (Fig. 1).

Two additional partial melting experiments were performed at 1.5 GPa using graphite (called S-Graph) and Re (called S-Re2) capsules. One layer of silicate powder with the composition of glasses from "Graph-1400" and "Re2-1370" experiments was sandwiched between two layers of the peridotite MPY-90 with 3% of IrO_2 added. The sandwich experiments were run for 49 h at the same conditions as the original experiments (i.e. 1400 °C for "S-Graph" and 1370 °C for "S-Re2"). BSE-images of these sandwich-experiments are shown in the electronic annex (Fig. EA1).

Supplementary data associated with this article can be found, in the online version, at https://doi.org/10.1016/j.gca.2018.07.019.

2.3. Synthesis of spinel and glass standards

A set of eight well-characterized natural spinels from different settings (Ionov and Wood, 1992) that covered a wide range of Fe^{3+} contents (between 0.1 and 0.35 $Fe^{3+}/\Sigma Fe$) were selected as standards for XANES-measurements. To extend this $Fe^{3+}/\Sigma Fe$ range, we synthesized 3 spinels at 1.5 GPa and 1400 °C at different fO_2 conditions using a piston cylinder apparatus. Different capsule materials were employed to apply different fO_2 conditions (cf. Section 2.2). Starting compositions for these synthetic spinel standards were taken from analyses of our MPY-90 pyrolite melting experiments, (i.e. Graph-1400, Re1-1400 and AuPd2-1370 in Table 2). In order to ensure chemical homogeneity of the resulting spinels, starting materials were synthesized using a sol–gel auto-combustion method (Vader et al., 2013).

Five silicate glass standards were also synthesized using a 1-atm gas mixing furnace at distinct fO_2 conditions between FMQ-2 and air. Oxygen fugacities were constrained from the CO-CO_2 gas mixtures (Chase, 1998) and confirmed to be identical within error to those measured with a $CaO–Y_2O_3$-stabilized ZrO_2 solid electrolyte cell. We used a natural picritic basalt as the starting material (SE1; Schuth et al., 2004) as its composition was comparable to glasses encountered in the partial melting experiments. We employed the wire-loop technique (e.g. Borisov et al., 1994; Laurenz et al., 2010) where the powdered picritic basalt was glued onto a Re or Pt wire-loop (depending on fO_2 conditions – cf. Borisov and Jones, 1999) and suspended in the hot zone of the furnace at 1300 °C. The temperature of the furnace was controlled using a Type S (Pt - $Pt_{90}Rh_{10}$) thermocouple. After a run time of 24 h, experiments were drop-quenched in water.

2.4. Sample preparation

After HP/HT experiments, capsules were cut in half and polished for electron microprobe analysis. The 12 experiments that contained the largest melt pockets were selected for XANES measurements and prepared by double polishing to a thickness of 30 μm. In order to be mounted onto the sample holder, the samples were sandwiched between two Ultralene® foils (a low X-ray absorption polymer). Eight of these sample sections were subsequently also analysed using Fourier Transform Infra-Red spectroscopy (FTIR).

Spinel and glass standards were first prepared for Mössbauer analysis by double polishing to a thickness of ~150 μm and ~280 μm, respectively. The thicknesses were predetermined from the chemical compositions and densities designed to optimize signal and beam absorption. For subsequent XANES analyses the standards were further double polished down to a thickness of 30 μm to be consistent with the samples.

3. ANALYTICAL METHODS

3.1. Quantification of major and minor element compositions and water analyses

Major and minor element compositions of coexisting phases were analysed using a JEOL JXA-8200 electron microprobe in wavelength dispersive mode (WDS). Analyses were carried out with 15 kV acceleration voltage and counting times of 20 s for Ni, Mn, Cr and Ti, and 10 s for all other elements. Mineral analyses were carried out using a 15 nA probe current and a focussed beam, while for glasses the beam current was lowered to 8 nA and a variable beam diameter between 3 and 20 μm was used, depending on the size of the melt pockets. A basalt glass standard BCR-2G (USGS) was used as a reference material for SiO_2 analyses of experimental glasses, whereas andradite was used for minerals. Other standards were andradite for Ca, spinel for Mg, $MnTiO_3$ for Ti and Mn and albite for Na. Pure metal standards were used for Fe, Ni and Cr. Matrix corrections were performed using the ($\phi\rho$)-z correction method. Additional internal spinel standards were employed to check the validity of estimates of spinel Fe^{3+} contents from stoichiometry. AuPd and FeIr alloy-compositions were measured with a 20 kV acceleration voltage and a 10 nA focused beam. The counting time was 30 s for all elements except Fe and Si which were measured for 60 s. The latter was analysed to monitor possible contributions to the signal by secondary fluorescence from surrounding silicates. Pure metal standards were employed with the exception of Si for which andradite was used. Matrix corrections were performed using the ZAF-correction method. Major and minor element compositions of glasses, minerals and alloys are summarized in Tables 2 and 3.

Water contents of glasses were measured using a Bruker IFS 120 FTIR spectrometer in conjunction with a Bruker IR microscope containing all-reflecting Cassegranian optics. The spectrometer is equipped with a permanent aligned Michelson-type interferometer with a 30° angle of incidence on the beamsplitter and a frequency-stabilized HeNe laser. Spectra were acquired from 200 scans with 4 cm^{-1} resolution using a tungsten light source, CaF_2-beamsplitter, and narrow-band MCT detector. A representative FTIR-spectrum is shown in the electronic annex (Fig. EA 2).

Table 2
Composition and proportion (in wt%) of experimental phases normalized to 100% anhydrous.

Sample	Run time (h)	SiO_2	2σ	TiO_2	2σ	Al_2O_3	2σ	Cr_2O_3	2σ	FeO	2σ	MnO	2σ	MgO	2σ	CaO	2σ	Na_2O	2σ	NiO	2σ	Sum[b]	Mg#[c]	H_2O	2σ	Bulk H_2O (wt. %)	2σ	Phase prop[d]		FeO loss[e]	$R^{2[f]}$
MPY-90[a]		44.74	*0.32*	0.17	*0.01*	4.37	*0.06*	0.45	*0.02*	7.55	*0.11*	0.11	*0.00*	38.57	*0.74*	3.38	*0.05*	0.40	*0.03*	0.26	*0.00*	100.00	90.11								
Graph-1320	49																													0.00	0.9
gl		49.14	*0.25*	1.40	*0.03*	18.50	*0.12*	0.06	*0.03*	6.83	*0.10*	0.11	*0.03*	10.59	*0.32*	9.17	*0.15*	4.16	*0.19*	0.03	*0.06*	95.50	73.42					5.60	*0.77*		
ol		40.67	*0.27*	0.02	*0.02*	0.19	*0.15*	0.07	*0.03*	9.38	*0.09*	0.12	*0.03*	48.92	*0.32*	0.25	*0.05*	0.03	*0.03*	0.35	*0.10*	101.32	90.29					58.75	*0.80*		
opx		53.23	*0.54*	0.20	*0.05*	6.88	*0.75*	0.49	*0.06*	5.73	*0.08*	0.11	*0.03*	31.06	*0.28*	2.01	*0.18*	0.18	*0.01*	0.11	*0.04*	100.55	90.62					16.34	*0.67*		
cpx		51.74	*0.79*	0.36	*0.07*	7.76	*1.16*	0.81	*0.30*	4.39	*0.35*	0.11	*0.04*	20.36	*1.36*	13.52	*1.52*	0.87	*0.14*	0.07	*0.03*	100.47	89.20					17.84	*0.74*		
spi		0.62	*0.16*	0.26	*0.03*	52.87	*2.85*	15.17	*3.47*	9.03	*0.43*	0.08	*0.05*	21.60	*0.49*	0.10	*0.04*	0.01	*0.02*	0.27	*0.08*	100.09						1.42	*0.07*		
Graph-1370	40																													0.00	2.0
gl		47.51	*0.22*	1.14	*0.07*	17.16	*0.14*	0.12	*0.02*	7.43	*0.12*	0.12	*0.04*	13.01	*0.16*	10.73	*0.12*	2.77	*0.08*	0.00	*0.01*	97.47	75.74	0.08	*0.02*	0.007	*0.002*	9.33	*0.53*		
ol		40.34	*0.21*	0.02	*0.02*	0.12	*0.02*	0.11	*0.03*	9.15	*0.05*	0.13	*0.03*	49.77	*0.28*	0.28	*0.03*	0.02	*0.02*	0.07	*0.05*	101.35	90.65					57.21	*2.49*		
opx		52.60	*0.65*	0.15	*0.02*	7.32	*0.74*	0.58	*0.08*	5.45	*0.07*	0.11	*0.04*	31.24	*0.35*	2.30	*0.04*	0.15	*0.02*	0.09	*0.06*	100.65	91.08					15.93	*2.67*		
cpx		51.41	*0.55*	0.25	*0.05*	8.07	*0.58*	0.74	*0.20*	4.44	*0.20*	0.12	*0.04*	22.27	*0.99*	12.10	*0.77*	0.57	*0.09*	0.02	*0.02*	100.21	89.93					16.80	*0.04*		
spi		0.26	*0.00*	0.14	*0.03*	60.83	*0.03*	7.92	*0.16*	7.45	*0.04*	0.07	*0.01*	23.18	*0.19*	0.06	*0.01*	0.01	*0.01*	0.09	*0.04*	100.26						0.49	*0.19*		
Graph-1400	24																													0.13	1.8
gl		47.49	*0.17*	1.08	*0.05*	17.82	*0.21*	0.08	*0.04*	7.18	*0.20*	0.14	*0.04*	12.57	*0.31*	11.00	*0.18*	2.61	*0.13*	0.03	*0.03*	97.77	75.72	0.16	*0.03*	0.018	*0.006*	11.44	*2.70*		
ol		39.86	*0.20*	0.02	*0.02*	0.13	*0.04*	0.10	*0.03*	9.00	*0.16*	0.12	*0.03*	50.39	*0.23*	0.29	*0.02*	0.02	*0.02*	0.07	*0.06*	99.77	90.89					54.66	*1.63*		
opx		52.57	*0.98*	0.11	*0.06*	6.45	*1.51*	0.74	*0.14*	5.31	*0.20*	0.11	*0.03*	32.14	*1.41*	2.43	*0.17*	0.11	*0.02*	0.03	*0.05*	98.84	91.52					20.52	*3.28*		
cpx		50.99	*0.38*	0.19	*0.03*	7.92	*0.38*	0.89	*0.18*	4.44	*0.14*	0.12	*0.03*	23.04	*0.61*	11.98	*0.62*	0.42	*0.05*	0.02	*0.03*	98.63	90.25					13.35	*0.80*		
spi		0.24	*0.06*	0.15	*0.03*	57.80	*1.25*	11.63	*1.39*	7.57	*0.10*	0.11	*0.02*	22.32	*0.20*	0.03	*0.02*	0.01	*0.01*	0.15	*0.08*	99.35						0.36	*0.23*		
Graph-1450	24																													1.17	2.6
gl		47.05	*0.29*	0.92	*0.07*	15.31	*0.35*	0.23	*0.04*	7.92	*0.34*	0.13	*0.04*	15.12	*0.44*	11.70	*0.21*	1.57	*0.07*	0.04	*0.04*	99.73	77.29	0.05	*0.03*	0.007	*0.004*	14.25	*1.46*		
ol		39.75	*0.22*	0.02	*0.02*	0.14	*0.06*	0.12	*0.04*	8.02	*0.39*	0.11	*0.03*	51.52	*0.40*	0.28	*0.04*	0.02	*0.02*	0.03	*0.04*	99.85	91.97					48.51	*2.80*		
opx		52.18	*0.65*	0.10	*0.02*	7.28	*0.74*	0.99	*0.08*	4.60	*0.07*	0.07	*0.04*	32.29	*0.35*	2.35	*0.04*	0.09	*0.02*	0.05	*0.06*	99.12	92.60					29.53	*3.76*		
cpx		50.88	*0.60*	0.20	*0.03*	7.52	*0.67*	1.10	*0.38*	4.23	*0.16*	0.12	*0.02*	23.63	*1.04*	11.88	*1.07*	0.43	*0.06*	0.02	*0.02*	98.45	90.88					7.36	*2.58*		
spi		0.26	*0.02*	0.18	*0.03*	58.00	*1.17*	11.12	*1.28*	6.96	*0.12*	0.08	*0.03*	23.30	*0.12*	0.04	*0.05*	0.03	*0.01*	0.03	*0.03*	100.08						0.00	*0.52*		
Re1-1320	50																													1.04	1.2
gl		48.79	*0.49*	0.97	*0.06*	17.43	*0.59*	0.12	*0.04*	5.40	*0.24*	0.13	*0.04*	13.29	*0.46*	11.83	*0.37*	2.02	*0.10*	0.02	*0.02*	93.31	81.43					10.61	*1.85*		
ol		39.93	*0.19*	0.01	*0.01*	0.09	*0.03*	0.09	*0.02*	8.03	*0.10*	0.11	*0.04*	51.13	*0.15*	0.23	*0.02*	0.01	*0.01*	0.38	*0.05*	99.54	91.90					50.92	*1.48*		
opx		52.00	*0.68*	0.17	*0.03*	7.50	*1.07*	0.75	*0.10*	5.50	*0.14*	0.10	*0.03*	31.59	*0.54*	2.14	*0.14*	0.10	*0.02*	0.15	*0.03*	98.63	91.11					28.57	*0.23*		
cpx		50.89	*0.18*	0.25	*0.03*	7.03	*0.24*	1.10	*0.08*	3.65	*0.18*	0.11	*0.03*	20.11	*0.42*	16.28	*0.55*	0.52	*0.03*	0.07	*0.03*	97.88	90.75					9.36	*1.27*		
spi		0.25	*0.11*	0.16	*0.02*	53.27	*1.58*	15.86	*1.58*	7.81	*0.14*	0.08	*0.03*	22.21	*0.31*	0.06	*0.03*	0.01	*0.01*	0.30	*0.05*	99.24						0.15	*0.21*		
Re1-1340	48																													1.30	0.6
gl		48.27	*0.24*	0.92	*0.05*	15.04	*0.19*	0.11	*0.02*	6.67	*0.13*	0.14	*0.05*	14.56	*0.55*	12.14	*0.27*	2.12	*0.22*	0.03	*0.02*	94.12	79.55					15.30	*0.69*		
ol		40.02	*0.14*	0.02	*0.01*	0.11	*0.01*	0.08	*0.02*	7.17	*0.15*	0.12	*0.03*	51.88	*0.17*	0.24	*0.02*	0.02	*0.01*	0.35	*0.05*	99.81	92.81					49.38	*1.64*		
opx		52.65	*0.70*	0.09	*0.04*	5.92	*0.61*	1.01	*0.11*	5.16	*0.19*	0.11	*0.04*	32.33	*0.65*	2.49	*0.34*	0.11	*0.03*	0.12	*0.03*	98.84	91.78					29.12	*1.06*		
cpx		50.66	*0.49*	0.15	*0.02*	6.50	*0.30*	1.22	*0.10*	4.20	*0.14*	0.11	*0.05*	21.86	*1.29*	14.71	*0.57*	0.50	*0.04*	0.10	*0.04*	98.39	90.28					5.44	*0.27*		
spi		0.24	*0.10*	0.20	*0.02*	44.31	*2.19*	22.07	*2.41*	11.32	*0.25*	0.11	*0.03*	21.36	*0.35*	0.06	*0.04*	0.00	*0.01*	0.32	*0.04*	99.24						0.16	*0.06*		
Re1-1370	30																													0.31	0.5
gl		47.76	*0.19*	0.81	*0.06*	14.75	*0.06*	0.15	*0.01*	7.61	*0.06*	0.19	*0.01*	14.79	*0.11*	12.04	*0.05*	1.89	*0.06*	0.03	*0.03*	96.60	77.60					18.25	*1.00*		
ol		40.20	*0.39*	0.01	*0.01*	0.16	*0.17*	0.09	*0.03*	8.06	*0.22*	0.12	*0.03*	50.71	*0.61*	0.27	*0.05*	0.01	*0.01*	0.36	*0.04*	101.04	91.81					54.30	*0.63*		
opx		53.01	*0.78*	0.09	*0.03*	5.88	*0.75*	1.07	*0.20*	5.36	*0.19*	0.11	*0.03*	31.66	*1.03*	2.59	*0.45*	0.12	*0.06*	0.11	*0.04*	100.39	91.32					23.04	*0.77*		
cpx		51.43	*0.46*	0.15	*0.03*	6.70	*0.37*	1.21	*0.12*	4.50	*0.16*	0.13	*0.04*	21.87	*1.04*	13.43	*1.16*	0.49	*0.03*	0.09	*0.04*	100.24	89.65					3.81	*0.87*		
spi		0.47	*0.12*	0.18	*0.02*	43.98	*1.26*	22.03	*1.22*	11.89	*0.18*	0.11	*0.02*	20.97	*0.19*	0.07	*0.03*	0.01	*0.01*	0.30	*0.05*	100.44						0.32	*0.06*		
Re1-1400	24																													1.94	1.3
gl		49.39	*0.31*	0.61	*0.07*	13.49	*0.83*	0.34	*0.04*	6.01	*0.14*	0.14	*0.05*	16.13	*0.37*	12.65	*0.66*	1.18	*0.11*	0.03	*0.04*	95.74	82.70					26.04	*2.60*		
ol		40.32	*0.14*	0.01	*0.01*	0.10	*0.02*	0.17	*0.03*	6.21	*0.11*	0.11	*0.03*	52.51	*0.17*	0.27	*0.02*	0.02	*0.01*	0.29	*0.04*	99.55	93.78					52.30	*2.32*		
opx		53.63	*0.80*	0.06	*0.02*	4.61	*0.95*	1.36	*0.22*	4.67	*0.23*	0.11	*0.03*	32.84	*1.31*	2.53	*0.18*	0.09	*0.02*	0.11	*0.03*	98.68	92.62					20.73	*6.87*		
spi		0.26	*0.14*	0.18	*0.01*	36.78	*2.92*	32.34	*3.10*	9.10	*0.17*	0.11	*0.04*	20.89	*0.39*	0.11	*0.09*	0.01	*0.01*	0.23	*0.03*	98.88						0.16	*0.24*		
Re1-1440	24																													0.96	1.5
gl		48.89	*0.28*	0.50	*0.04*	12.03	*0.23*	0.41	*0.03*	7.99	*0.09*	0.15	*0.06*	17.72	*0.30*	11.27	*0.14*	0.99	*0.04*	0.05	*0.05*	97.50	79.82					28.77	*1.77*		
ol		39.83	*0.30*	0.01	*0.01*	0.12	*0.02*	0.21	*0.04*	7.00	*0.10*	0.10	*0.03*	52.06	*0.21*	0.28	*0.02*	0.01	*0.01*	0.38	*0.05*	99.81	92.98					51.76	*2.72*		
opx		54.22	*0.84*	0.04	*0.02*	3.38	*0.44*	1.50	*0.17*	4.66	*0.10*	0.10	*0.03*	34.11	*0.53*	1.80	*0.06*	0.06	*0.02*	0.14	*0.03*	99.01	92.88					19.23	*4.06*		
spi		0.21	*0.15*	0.18	*0.03*	23.54	*0.83*	44.66	*0.91*	11.90	*0.10*	0.16	*0.03*	18.96	*0.14*	0.16	*0.07*	0.01	*0.01*	0.22	*0.03*	99.25						0.01	*0.15*		

(*continued on next page*)

Table 2 (*continued*)

Sample	Run time (h)	SiO_2	2σ	TiO_2	2σ	Al_2O_3	2σ	Cr_2O_3	2σ	FeO	2σ	MnO	2σ	MgO	2σ	CaO	2σ	Na_2O	2σ	NiO	2σ	Sum[b]	Mg#[c]	H_2O	2σ	Bulk H_2O (wt. %)	2σ	Phase prop[d]		FeO loss[e]	R[2f]
Re2-1320	50																													0.14	1.3
gl		47.56	*0.17*	1.15	*0.07*	16.12	*0.10*	0.08	*0.03*	8.29	*0.09*	0.13	*0.04*	12.93	*0.21*	11.65	*0.16*	2.04	*0.07*	0.04	*0.05*	94.94	73.55					11.14	*2.16*		
ol		39.55	*0.18*	0.01	*0.01*	0.13	*0.08*	0.06	*0.04*	8.58	*0.12*	0.11	*0.03*	50.93	*0.20*	0.26	*0.05*	0.01	*0.01*	0.36	*0.04*	99.82	91.37					51.20	*1.54*		
opx		52.13	*0.49*	0.13	*0.03*	6.64	*0.62*	0.67	*0.08*	5.90	*0.14*	0.10	*0.04*	31.99	*0.25*	2.20	*0.08*	0.10	*0.02*	0.13	*0.05*	99.04	90.62					28.55	*1.92*		
cpx		49.77	*0.38*	0.24	*0.03*	7.71	*0.40*	0.81	*0.14*	4.87	*0.30*	0.09	*0.04*	20.35	*0.52*	15.58	*0.66*	0.51	*0.06*	0.08	*0.04*	98.65	88.16					9.00	*1.46*		
spi		0.33	*0.14*	0.19	*0.02*	52.22	*1.27*	12.04	*1.22*	12.75	*0.21*	0.09	*0.04*	21.91	*0.38*	0.06	*0.02*	0.01	*0.01*	0.40	*0.04*	100.17						0.24	*0.40*		
Re2-1370	30																													0.82	0.7
gl		48.44	*0.65*	0.66	*0.06*	16.06	*0.84*	0.14	*0.03*	8.47	*0.28*	0.18	*0.05*	12.14	*1.90*	12.13	*1.20*	1.79	*0.32*	0.00	*0.02*	94.41	71.86					22.38	*2.04*		
ol		40.17	*0.22*	0.02	*0.02*	0.10	*0.01*	0.09	*0.02*	7.31	*0.06*	0.11	*0.03*	51.57	*0.31*	0.26	*0.04*	0.01	*0.01*	0.37	*0.05*	99.54	92.64					54.00	*2.26*		
opx		53.98	*0.49*	0.05	*0.02*	4.03	*0.38*	1.35	*0.12*	4.84	*0.07*	0.10	*0.03*	33.33	*0.50*	2.15	*0.18*	0.06	*0.02*	0.12	*0.03*	98.39	92.47					22.74	*2.83*		
cpx		50.62	*0.40*	0.13	*0.03*	6.89	*0.39*	1.12	*0.08*	4.12	*0.14*	0.10	*0.03*	20.66	*0.56*	15.91	*0.58*	0.36	*0.02*	0.09	*0.03*	98.20	89.94					0.81	*1.29*		
spi		0.21	*0.06*	0.16	*0.01*	34.74	*0.76*	31.11	*0.75*	13.31	*0.13*	0.13	*0.02*	19.94	*0.25*	0.10	*0.04*	0.01	*0.01*	0.30	*0.04*	98.27						0.18	*0.13*		
Re2-1400	24																													1.51	1.5
gl		49.11	*0.39*	0.49	*0.04*	12.09	*0.47*	0.34	*0.04*	7.18	*0.11*	0.14	*0.06*	17.87	*0.50*	11.60	*0.16*	1.10	*0.04*	0.07	*0.04*	95.81	81.61					30.66	*4.12*		
ol		40.34	*0.26*	0.01	*0.01*	0.10	*0.02*	0.16	*0.02*	6.41	*0.09*	0.10	*0.04*	52.30	*0.28*	0.22	*0.01*	0.01	*0.01*	0.34	*0.04*	100.64	93.57					52.19	*2.02*		
opx		54.77	*0.73*	0.06	*0.03*	3.34	*0.11*	1.34	*0.04*	4.25	*0.15*	0.12	*0.03*	34.26	*0.45*	1.68	*0.08*	0.06	*0.01*	0.12	*0.05*	100.06	93.49					16.29	*5.48*		
spi		0.46	*0.63*	0.15	*0.02*	22.32	*0.67*	46.28	*1.31*	11.19	*0.09*	0.15	*0.02*	19.12	*0.21*	0.12	*0.17*	0.02	*0.03*	0.20	*0.03*	99.36						0.18	*0.16*		
Re2-1440	24																													0.26	1.2
gl		49.90	*0.88*	0.43	*0.05*	11.01	*0.76*	0.45	*0.16*	8.26	*0.33*	0.13	*0.05*	18.63	*0.60*	10.20	*0.92*	0.91	*0.06*	0.07	*0.05*	95.39	80.08	0.44	*0.04*	0.19	*0.02*	42.17	*0.73*		
ol		40.07	*0.29*	0.01	*0.01*	0.12	*0.05*	0.25	*0.03*	6.72	*0.06*	0.10	*0.03*	52.13	*0.47*	0.21	*0.04*	0.01	*0.01*	0.37	*0.04*	99.43	93.25					58.71	*1.41*		
spi		0.25	*0.07*	0.15	*0.02*	20.50	*0.27*	48.06	*0.19*	11.92	*0.09*	0.12	*0.03*	18.68	*0.12*	0.09	*0.03*	0.01	*0.01*	0.23	*0.04*	98.22						0.04	*0.16*		
AuPd1-1310	48																													0.71	1.7
gl		47.92	*0.16*	1.47	*0.05*	17.43	*0.08*	0.03	*0.01*	7.31	*0.11*	0.14	*0.06*	12.16	*0.10*	10.39	*0.12*	3.15	*0.06*	0.02	*0.03*	95.86	74.76	0.69	*0.07*	0.036	*0.005*	5.17	*0.45*		
ol		39.77	*0.23*	0.02	*0.02*	0.15	*0.10*	0.05	*0.02*	7.94	*0.17*	0.11	*0.02*	51.50	*0.42*	0.25	*0.02*	0.02	*0.01*	0.20	*0.06*	99.49	92.04					50.59	*1.80*		
opx		51.66	*0.49*	0.17	*0.02*	7.39	*0.48*	0.59	*0.11*	5.81	*0.13*	0.11	*0.03*	31.77	*0.54*	2.29	*0.23*	0.13	*0.02*	0.08	*0.05*	98.38	90.69					31.08	*1.87*		
cpx		49.95	*0.36*	0.37	*0.04*	8.32	*0.36*	0.51	*0.09*	4.43	*0.17*	0.12	*0.03*	19.77	*0.86*	15.69	*0.73*	0.80	*0.06*	0.04	*0.03*	97.70	88.83					13.38	*0.00*		
spi		0.29	*0.15*	0.20	*0.02*	57.82	*1.26*	6.61	*1.15*	11.43	*0.33*	0.09	*0.03*	23.28	*0.30*	0.10	*0.02*	0.00	*0.01*	0.17	*0.04*	100.17						0.39	*0.41*		
AuPd1-1330	48																													0.64	1.0
gl		47.09	*0.32*	1.24	*0.03*	17.68	*0.08*	0.02	*0.02*	7.24	*0.09*	0.13	*0.05*	12.86	*0.07*	11.03	*0.07*	2.69	*0.08*	0.02	*0.03*	95.89	76.00	0.73	*0.07*	0.07	*0.01*	10.26	*1.57*		
ol		39.31	*0.29*	0.01	*0.01*	0.17	*0.27*	0.06	*0.05*	8.18	*0.06*	0.11	*0.03*	51.61	*0.20*	0.24	*0.02*	0.01	*0.01*	0.30	*0.06*	99.78	91.84					49.15	*0.26*		
opx		51.93	*0.34*	0.11	*0.02*	6.65	*0.32*	0.94	*0.09*	5.56	*0.10*	0.08	*0.03*	32.10	*0.36*	2.42	*0.14*	0.12	*0.02*	0.10	*0.03*	98.83	91.14					30.62	*0.77*		
cpx		50.50	*0.38*	0.22	*0.03*	7.21	*0.29*	0.95	*0.09*	4.44	*0.15*	0.09	*0.04*	20.82	*0.95*	15.07	*1.02*	0.64	*0.02*	0.06	*0.03*	98.58	89.32					9.65	*1.14*		
spi		0.34	*0.15*	0.23	*0.02*	51.25	*0.27*	13.10	*0.15*	12.47	*0.12*	0.08	*0.04*	22.18	*0.24*	0.05	*0.03*	0.01	*0.01*	0.30	*0.04*	99.65						0.43	*0.28*		
AuPd1-1360	45																													0.45	2.1
gl		46.98	*0.28*	1.47	*0.05*	16.54	*0.13*	0.02	*0.01*	8.46	*0.24*	0.12	*0.02*	13.03	*0.09*	10.79	*0.10*	2.54	*0.09*	0.03	*0.04*	97.06	73.30					10.25	*6.50*		
ol		39.75	*0.25*	0.02	*0.02*	0.37	*0.31*	0.04	*0.03*	8.09	*0.14*	0.12	*0.02*	51.11	*0.39*	0.34	*0.15*	0.02	*0.01*	0.14	*0.04*	99.46	91.84					53.06	*2.97*		
opx		51.47	*0.57*	0.12	*0.02*	7.60	*0.40*	0.79	*0.08*	5.70	*0.18*	0.11	*0.01*	31.21	*0.76*	2.65	*0.34*	0.13	*0.03*	0.11	*0.05*	98.97	90.71					27.67	*4.76*		
cpx		50.18	*0.59*	0.33	*0.11*	8.74	*0.71*	0.43	*0.12*	4.93	*0.31*	0.12	*0.02*	20.46	*1.05*	14.12	*1.01*	0.66	*0.08*	0.05	*0.04*	98.41	88.10					9.84	*4.12*		
spi		0.30	*0.03*	0.21	*0.03*	56.84	*1.01*	7.10	*0.86*	12.37	*0.31*	0.09	*0.02*	22.74	*0.22*	0.09	*0.02*	0.01	*0.01*	0.26	*0.06*	99.73						0.52	*1.01*		
AuPd1-1390	24																													0.98	1.3
gl		48.73	*1.26*	0.80	*0.11*	16.55	*1.51*	0.07	*0.02*	6.96	*0.65*	0.11	*0.02*	11.41	*0.49*	13.77	*0.92*	1.59	*0.25*	0.01	*0.01*	97.05	74.52					19.86	*1.60*		
ol		39.98	*0.42*	0.01	*0.01*	0.16	*0.15*	0.14	*0.04*	7.22	*0.07*	0.10	*0.03*	51.81	*0.60*	0.32	*0.06*	0.01	*0.01*	0.25	*0.03*	100.27	92.75					53.63	*0.93*		
opx		53.08	*0.45*	0.07	*0.02*	4.56	*0.37*	1.40	*0.20*	5.08	*0.09*	0.09	*0.04*	32.89	*0.53*	2.61	*0.19*	0.07	*0.02*	0.14	*0.04*	99.47	92.03					25.96	*1.71*		
spi		0.25	*0.05*	0.17	*0.02*	34.71	*1.31*	32.67	*1.43*	11.43	*0.21*	0.11	*0.03*	20.36	*0.31*	0.07	*0.03*	0.00	*0.01*	0.21	*0.06*	99.64						0.07	*0.06*		
AuPd2-1320	48																													0.15	0.6
gl		46.37	*0.30*	0.79	*0.04*	12.15	*0.15*	0.08	*0.03*	12.09	*0.17*	0.14	*0.05*	15.09	*0.36*	11.43	*0.25*	1.81	*0.12*	0.05	*0.04*	95.53	68.98	0.85	*0.09*	0.11	*0.04*	12.56	*4.84*		
ol		39.43	*0.26*	0.01	*0.01*	0.12	*0.04*	0.04	*0.02*	4.15	*0.10*	0.11	*0.03*	55.47	*0.32*	0.24	*0.02*	0.01	*0.01*	0.41	*0.05*	98.42	95.98					37.75	*3.29*		
opx		52.24	*0.57*	0.06	*0.02*	4.70	*0.45*	0.31	*0.05*	5.46	*0.34*	0.11	*0.03*	34.56	*0.47*	2.33	*0.21*	0.11	*0.02*	0.13	*0.03*	97.43	91.86					42.17	*3.43*		
cpx		48.68	*0.51*	0.14	*0.03*	5.93	*0.29*	0.33	*0.05*	6.46	*0.20*	0.11	*0.04*	20.21	*0.70*	17.40	*0.50*	0.65	*0.07*	0.09	*0.03*	96.16	84.79					5.59	*2.43*		
spi		0.25	*0.05*	0.35	*0.02*	20.49	*0.54*	8.80	*0.75*	49.19	*0.47*	0.16	*0.03*	19.98	*0.19*	0.08	*0.05*	0.01	*0.01*	0.68	*0.04*	95.22						3.56	*0.98*		
AuPd2-1330	48																													0.00	0.6
gl		46.79	*0.20*	0.71	*0.06*	12.27	*0.08*	0.08	*0.02*	12.02	*0.29*	0.13	*0.02*	14.65	*0.12*	11.76	*0.08*	1.54	*0.05*	0.05	*0.04*	96.14	68.48	0.69	*0.07*	0.13	*0.02*	18.76	*1.79*		
ol		40.82	*0.40*	0.01	*0.02*	0.12	*0.01*	0.04	*0.01*	4.63	*0.11*	0.10	*0.02*	53.61	*0.26*	0.25	*0.02*	0.01	*0.01*	0.41	*0.04*	99.67	95.38					46.98	*1.61*		
opx		53.59	*0.68*	0.06	*0.03*	4.78	*0.57*	0.23	*0.08*	5.46	*0.41*	0.10	*0.02*	33.30	*0.54*	2.25	*0.10*	0.09	*0.02*	0.13	*0.04*	98.89	91.57					29.24	*1.67*		
cpx		50.65	*0.57*	0.13	*0.01*	5.56	*0.40*	0.34	*0.03*	6.03	*0.27*	0.09	*0.02*	19.71	*0.61*	16.87	*0.36*	0.54	*0.04*	0.08	*0.03*	98.69	85.35					2.86	*0.93*		
spi		0.26	*0.03*	0.32	*0.02*	21.42	*0.25*	10.71	*0.43*	47.02	*0.27*	0.17	*0.03*	19.39	*0.13*	0.12	*0.03*	0.01	*0.01*	0.59	*0.06*	94.86						3.17	*0.16*		

AuPd2-1350	30																									0.00	0.6
gl		46.29	*1.17*	0.69	*0.04*	10.96	*0.73*	0.12	*0.04*	11.86	*0.87*	0.18	*0.01*	15.68	*1.52*	13.05	*0.50*	1.12	*0.74*	0.05	*0.08*	96.88	70.21	17.86	*0.88*		
ol		40.94	*0.27*	0.01	*0.01*	0.13	*0.06*	0.04	*0.02*	3.34	*0.10*	0.11	*0.02*	54.76	*0.38*	0.25	*0.03*	0.01	*0.01*	0.41	*0.05*	99.86	96.69	40.94	*0.80*		
opx		53.51	*0.43*	0.05	*0.02*	4.28	*0.33*	0.36	*0.04*	5.04	*0.27*	0.10	*0.02*	34.24	*0.34*	2.22	*0.13*	0.08	*0.02*	0.13	*0.04*	99.24	92.38	35.90	*0.63*		
cpx		50.95	*0.59*	0.10	*0.03*	4.89	*0.43*	0.42	*0.04*	5.59	*0.29*	0.10	*0.02*	21.01	*0.89*	16.29	*0.66*	0.54	*0.05*	0.10	*0.04*	98.69	87.01	1.40	*0.42*		
spi		0.28	*0.05*	0.40	*0.03*	21.40	*0.61*	5.66	*0.53*	50.66	*0.46*	0.19	*0.02*	20.54	*0.24*	0.12	*0.03*	0.01	*0.01*	0.74	*0.05*	94.86		4.51	*0.44*		
AuPd2-1370	24																									0.40	1.3
gl		47.01	*0.19*	0.48	*0.04*	11.36	*0.34*	0.14	*0.04*	12.36	*0.35*	0.13	*0.05*	15.50	*1.68*	11.80	*0.32*	1.13	*0.22*	0.08	*0.04*	96.56	69.09	24.51	*0.63*		
ol		40.42	*0.26*	0.01	*0.01*	0.12	*0.07*	0.06	*0.03*	4.47	*0.06*	0.10	*0.04*	54.17	*0.41*	0.24	*0.03*	0.01	*0.01*	0.40	*0.04*	99.91	95.57	44.72	*0.79*		
opx		53.70	*0.43*	0.04	*0.02*	3.80	*0.41*	0.46	*0.05*	5.11	*0.32*	0.10	*0.03*	34.59	*0.52*	2.00	*0.15*	0.07	*0.03*	0.13	*0.04*	99.35	92.35	28.73	*0.28*		
spi		0.20	*0.02*	0.19	*0.02*	18.07	*0.13*	16.83	*0.19*	44.43	*0.32*	0.18	*0.03*	19.42	*0.09*	0.09	*0.04*	0.00	*0.00*	0.59	*0.04*	95.75		2.27	*0.57*		

Numbers next to the sample names indicate the temperatures of the experiements.

Numbers in italic are 2σ analytical error.

gl = glass, ol = olivine, opx = orthopyroxene, cpx = clinopyroxene, spi = spinel.

[a] Composition of starting material MPY-90 from Falloon and Green (1987) measured using ICP-AES.

[b] Initial analytical total.

[c] Molar ratio [100 * Mg/(Mg + Fe2+)].

[d] Phase proportion calculated by mass balance program (Albarède and Provost, 1977).

[e] Relative iron loss calculated by mass balance

[f] Sum of the square residuals.

3.2. Mössbauer spectroscopy of standards and sandwich experiments

Mössbauer spectra for the spinel and glass standards, as well as the glass layers present in sandwich-experiments were recorded at room temperature in transmission mode on a constant acceleration Mössbauer spectrometer with a nominal 450 MBq ^{57}Co high specific activity source in a 12 μm thick Rh matrix. The velocity scales were calibrated relative to 25 μm thick α-Fe foil using the positions certified for standard reference material no. 1541 of the (former) National Bureau of Standards. Line widths of 0.36 mm/s for the outer lines of α-Fe were obtained at room temperature. Measurement times for each spectrum varied from 1 to 3 days. Spectra were fitted using the program MossA (Prescher et al., 2012). The Mössbauer spectra of the spinels were fitted with three Lorentzian doublets, two for Fe^{2+} and one for Fe^{3+}, in a similar procedure to that described by Wood and Virgo (1989). An equal area and width constraint was applied for both components of each individual doublet (Fig. EA 3 a-d).

Due to the broader Mössbauer spectra of the glasses and the potential for peak overlap, different fitting models were applied based on the extended Voigt-based fitting (xVBF) approach (e.g., Alberto et al., 1996; Lagarec and Rancourt, 1997) (Fig. EA3 e-h). For the SE1-FE6 standard, where the spectrum is clearly dominated by Fe^{3+}, fitting was performed using two doublets (Pseudo-Voigt lineshape) for Fe^{3+} and one doublet (xVBF model) for Fe^{2+} (e.g., Partzsch et al., 2004). Glass spectra showing intermediate Fe^{3+} contents ($Fe^{3+}/\Sigma Fe$ between 0.1 and 0.3, i.e., SE1-FE2 and SE1-FE1) were fitted with one doublet (Pseudo-Voigt lineshape) for Fe^{3+} with the linewidth fixed to 0.65 mm/s, and one doublet (xVBF model) for Fe^{2+}. The spectra for standards SE1-FE3 and SE1-FE4 do not show obvious features indicating Fe^{3+}, although it must be present because no statistically reasonable fits could be obtained using Fe^{2+} components alone. The best fitting model for these spectra employed one doublet (Pseudo-Voigt lineshape) for Fe^{3+} and two doublets (xVBF model) for Fe^{2+}. $Fe^{3+}/\Sigma Fe$ ratios were determined from the relative peak areas, assuming equal recoil-free fractions for Fe^{2+} and Fe^{3+} (e.g., Partzsch et al., 2004). Uncertainties (2σ) were estimated based on the statistical fitting errors and uncertainty in the fitting model itself.

3.3. Full-field XANES analyses

3.3.1. Data collection

Fe *K*-edge full-field XANES measurements (Fayard et al., 2013) were performed at the ID21 beamline of the European Synchrotron Radiation Facility (ESRF, Grenoble, France). Recent studies have emphasized the potential of recording X-ray absorption near edge structure (XANES) spectra using full-field absorption radiographies with a large X-ray beam, for polycrystalline and heterogeneous materials (De Andrade et al., 2011; Meirer et al., 2011, 2013; Gonzalez-Jimenez et al., 2012; Fayard et al., 2013; Pouyet et al., 2015). This setup allows the acquisition of stacks of more than 200 images at each energy step of the

Table 3
Compositions of the alloys present in the experiments (wt%).

Sample	Ir	2σ	Fe	2σ	Au	2σ	Pd	2σ	Total
Graph-1370	85.51	0.55	11.78	0.18					97.29
Graph-1400	90.27	0.46	8.12	0.17					98.39
Re1-1400	54.44	5.20	1.05	0.17					55.49
Re1-1440	66.41	1.16	1.06	0.35					67.47
AuPd1-1310			0.70	0.05	77.47	1.67	17.66	0.81	95.83
AuPd1-1330			0.23	0.03	80.66	0.52	17.39	0.26	98.27
AuPd2-1320			0.31	0.05	79.30	0.86	17.95	0.35	97.56
AuPd2-1330			0.28	0.03	79.61	0.71	17.26	0.25	97.15
AuPd2-1370			0.22	0.02	80.80	0.55	17.32	0.16	98.34

XANES spectrum range. Images are acquired spatially across the samples with a field of view from 600 × 600 μm^2 up to 2 × 2 mm^2 and pixel sizes between 0.3 and 1.4 μm. Each pixel contains a full high resolution XANES measurement. We chose this setup in order to improve the determination of Fe^{2+}/Fe^{3+} measurement in spinels by increasing the number of XANES spectra collected over a large field of view, in comparison to a classical focused beam setup. In the peridotite partial melting experiments, spinels are a minor phase (≤4.5% spinel, Table 2) and most of the crystals present have diameters of <10 μm. The large scale mapping coupled to the small pixel size offered by such a technique is, therefore, crucial for obtaining suitable statistics for the spinels XANES spectra. Additionally, this method allows subtle redox variations across the samples and within spinel single crystals to be determined.

A monochromatic X-ray beam was obtained using a fixed exit double-crystal monochromator (0.62 eV resolution at 7.2 keV). The monochromatic energy was calibrated against the first inflection point of a Fe foil (4 μm thick) spectrum at 7110.78 eV. The field of view covered by the CCD camera (CMOS PCO.edge) and selected for the acquisition was 0.8 mm^2 with a pixel size of 0.3 × 0.3 μm^2. Before and after each acquisition, a reference image was recorded (using the same experimental parameters), with the sample moved out of the X-ray beam. Further parameters of the XANES measurements are reported in Table 4.

3.3.2. Data processing and spectral fitting

Pre-processing of the full-field XANES data encompasses (i) intensity normalization of the transmitted images using reference images in order to correct for variations of the beam intensity at different energies caused by the X-ray optics stability, and (ii) image realignment in order to correct for possible short displacements of the sample in the field of view due to repositioning after reference image collection (Fig. 2a and e). The resulting stacks of images were then processed using the software application TXM-Wizard, developed to optimize the handling of large quantities of full-field XANES data (Liu et al., 2012). The first step in the image analysis is to determine the absorption edge jump, i.e. the average intensity difference between the post-edge and pre-edge regions. Pixels for which the Fe *K*-edge is not significant due to low Fe concentrations were removed. Pixel intensities in the resulting edge-jump maps reflect variations in Fe concentration (Fig. 2b and f). The XANES spectra for each pixel were then normalized by applying linear regressions that set the pre-edge region to an intensity value of 0 and the post-edge region to 1. During this step, pixels showing extreme slopes for the pre and post-edge line were removed. Following this normalization, the edge energy position was determined as the position at the half-height of the normalized edge, which corresponds to the 1 s–4 s transition between bound electronic states. Because transitions of this type shift to higher energy with increasing oxidation state (e.g., Wong et al., 1984; Sutton et al., 1993), maps of edge energy position provide information on the oxidation state of iron (Fig. 2c and g). Furthermore, principal component analysis (PCA) and subsequent *k*-means clustering were conducted, typically using 10 components and 2–6 clusters. The resulting maps combine information about iron distribution, crystal structure, orientation and valence state of iron by dividing the field of view in different clusters of pixels (Fig. 2d and h).

XANES spectra were subsequently extracted from selected regions of interest identified on the different maps (Fig. EA4 in the electronic Annex). Previous studies have indicated that the energy position of the pre-edge peak centroid appears to provide one of the best correlations with the $Fe^{3+}/\Sigma Fe$ ratio of the sample (e.g., Berry et al., 2003, 2010; Wilke et al., 2001, 2005). The pre-edges of glasses and spinel spectra were deconvoluted in the 7104–7120 eV energy range into two pseudo-Voigt peaks with equal width and with the Gaussian fraction fixed to 50% (Berry et al., 2008, 2010). This was performed simultaneously with background fitting to a single Voigt function (cf. Fig. EA5 in the

Table 4
Full field XANES parameters.

Energy range (ev)	Number of points	Step size (eV)	Number of images per point
7060–7100	20	2	10
7100–7116	40	0.4	24
7116–7142	78	0.3	10
7142–7162	40	0.5	10
7162–7192	15	2	10
7192–7350	32	5	10

Dark images: 31 img Acquisition time for each scan: 0.16 sec.

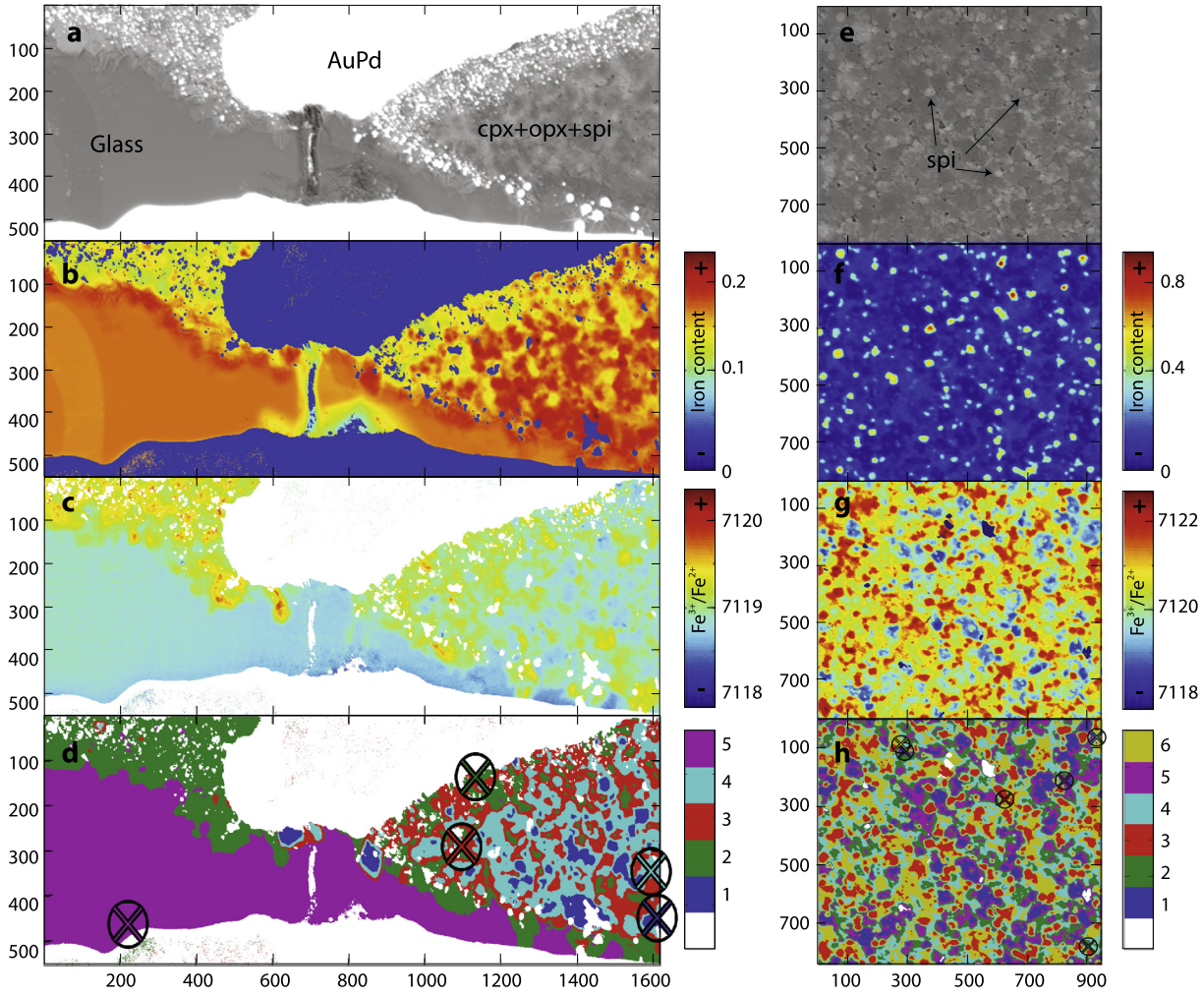

Fig. 2. TXM-Wizard maps generated from full-field XANES data collected on samples AuPd1-1310 (left images) and AuPd2-1320 (right images) showing a sequence of processed images of regions containing glass and spinels, respectively. (a, e) Transmission image recorded at 7080 eV after alignment and magnification correction. (b, f) Edge-jump map (numbers next to the colour bar are the difference between the average intensity in the post-edge region and the average intensity in the pre-edge region and reflect iron content). (c, g) Map of the edge energy position (numbers next to the color bar are the energy position at the half-height of the normalized edge, in eV). (d, h) PCA and *k*-means clustering: Glass is represented by cluster 5 (purple) on the left image, and spinel by cluster 3 (red) on the right image. The identified regions of interest are indicated by the black crosses (cf. Section 3.3). (For interpretation of the references to color in this figure legend, the reader is referred to the web version of this article.)

Electronic Annex), yielding the best fits to the observed spectra. For glasses, this model gave a better fit than models involving 4 Gaussian functions (Wilke et al., 2005) or additional pseudo-Voigt functions (Berry et al., 2008, 2010). The centroid was calculated as the area-weighted average of the pre-edge peak position. Two alternative methods to obtain $Fe^{3+}/\Sigma Fe$ correlations from XANES spectral properties were also tested and compared to the pre-edge peak centroid method: (i) The energy of the main absorption edge at a normalized height of 0.9 was employed (Berry et al., 2003, 2010), and (ii) the intensity ratio $I(Fe^{3+})/[I(Fe^{3+})+I(Fe^{2+})]$ was employed, where $I(Fe^{2+})$ and $I(Fe^{3+})$ are determined by integrating the extracted pre-edge spectra between 7110.5 and 7112.3 eV, and between 7112.5 and 7113.9 eV for the contribution of Fe^{2+} and Fe^{3+}, respectively (Wilke et al., 2005).

4. RESULTS

4.1. Textural observations and mineral and melt compositions

Mineral and melt proportions for each experiment were determined through a mass balance calculation (Albarède and Provost, 1977) employing the MPY-90 bulk composition. In each experiment, melt coexisted with a spinel peridotite assemblage with clinopyroxene being absent from the experiments performed under more oxidizing conditions above ~1360 °C ("Re", "AuPd1" and "AuPd2" series). Melts, which quenched predominantly to glass, could be easily recognized in all samples and were well separated from other phases due to the different melt extraction techniques employed (Fig. 1). At a given temperature, the proportion of melting increases with the general oxidation state of the

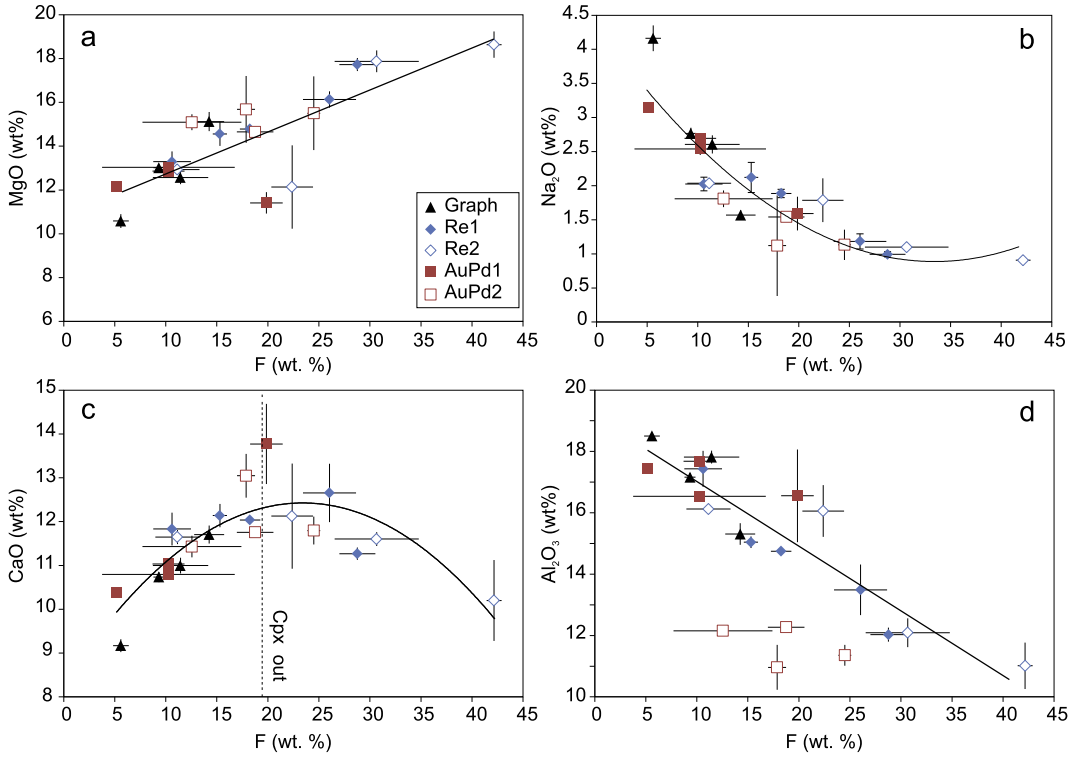

Fig. 3. Major element compositions of experimental glasses (with 2σ error bars) as a function of partial melting degree (F in wt%). Solid curves show the best fit to the entire data. The dashed line on (c) indicates the melt fraction at which clinopyroxene (cpx) is exhausted.

experiments. At 1370 °C, for example, a partial melting degree (F) equivalent to 10 wt% melt occurs for "Graph" experiments while ~25 wt% melt forms in "AuPd2" experiments.

With increasing partial melting degree, the MgO concentration of the melt increases from 10.6 to 18.6 wt%, Na_2O decreases from 4.2 to 0.9 wt% and the behaviour of CaO changes in relation to the presence of clinopyroxene (Fig. 3). For constant partial melting degree (F), MgO, CaO and Na_2O contents of melts are fairly homogeneous for all experiments, thus showing that fO_2 does not have a significant influence on the behaviour of these elements. In contrast, melts formed under the most oxidizing conditions in the "AuPd2" experiments have lower SiO_2 (46.6 wt% on average) and Al_2O_3 (11.7 wt%) contents, as well as higher FeO contents (12.1 wt%) compared to experiments at more reducing conditions, which have average concentrations of approximately 48, 16 and 7.5 wt% of SiO_2, Al_2O_3 and FeO, respectively.

Mineral phases are generally well equilibrated with only minor zonation recognized in the Ca content of some clinopyroxenes and the Cr-Al contents of spinels, as indicated by the standard deviations reported in Table 2. The Cr_2O_3 content of spinel is positively correlated to the partial melting degree in all experiments except those in the "AuPd-2" series, where spinels have overall lower Cr_2O_3 contents (10.5 wt%, Fig. 4a), likely due to the extremely high fO_2 conditions (Ballhaus et al., 1991). Spinels from AuPd2 experiments are also poorer in Al_2O_3 (20.3 wt%) and richer in FeO_{tot} (47.8 wt%) than spinels from experiments at lower fO_2.

Overall, the Mg# of olivine ($Mg/(Mg + Fe^{2+})$) varies from 0.90 to 0.96 while orthopyroxene Mg# varies from 0.96 to 0.94 and that of clinopyroxene varies from 0.85 to 0.91. Mg# for both olivine and orthopyroxene increases with fraction of melting, with the exception of the Mg# of olivine in the most oxidized AuPd2 experiments. Regardless of melting degree, the Mg# of olivine increases with fO_2 (Fig. 4b). The latter is caused by the formation of Fe^{3+} at high fO_2 conditions, which does not partition into olivine

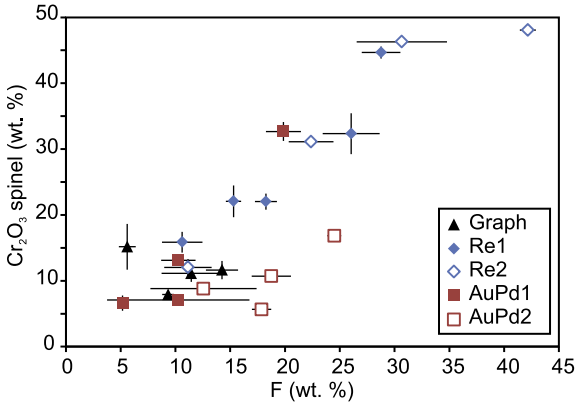

Fig. 4. (a) Cr_2O_3 content of spinel versus partial melting degree (F in wt%) and (b) Mg# [$Mg/(Mg + Fe^{2+})$] x100 of olivine as a function of fO_2 relative to the FMQ buffer (see Section 5.1 for details concerning the calculation of fO_2), from analyses of experimental run products.

so that highly forsteritic olivines are stabilized. The opposite effect can be seen for clinopyroxene, the Mg# of which decreases with increasing fO_2 because clinopyroxenes become increasingly Fe^{3+}-rich. There is no obvious correlation of the Mg# of orthopyroxene with fO_2.

4.2. $Fe^{3+}/\Sigma Fe$ ratio determinations of standards and experimental phases

The determined $Fe^{3+}/\Sigma Fe$ ratios of our synthetic glass standards measured by Mössbauer spectroscopy range from 0.07 ± 0.04 to 0.79 ± 0.04 (Table 5) and are in good agreement with those predicted from the fO_2 of synthesis (Kress and Carmichael, 1991). $Fe^{3+}/\Sigma Fe$ determined for the natural spinel standards are consistent with the previous results of Ionov and Wood (1992) for the same samples. The synthetic spinel standards Spi-graph, Spi-Re and Spi-AuPd have $Fe^{3+}/\Sigma Fe$ ratios of 0.50 ± 0.03, 0.68 ± 0.04 and 0.77 ± 0.02, respectively. These values compare well with the $Fe^{3+}/\Sigma Fe$ ratios of 0.6, 0.7 and 0.8 calculated by stoichiometry from electron microprobe measurements. The $Fe^{3+}/\Sigma Fe$ ratios of the glass layer present in sandwich-experiments measured by Mössbauer spectroscopy were 0.05 ± 0.04 for "S-Graph" and 0.12 ± 0.04 for "S-Re2"-experiments. As will be discussed later this is in good agreement with the expected oxygen fugacities for these experiments.

The best correlation between XANES spectra properties of the standards and $Fe^{3+}/\Sigma Fe$ ratios determined by Mössbauer was found for the pre-edge centroid for which the coefficient of correlation (R^2) is 1.00 for glasses and 0.98 for spinels (Fig. 5). Although the intensity ratios of the pre-edge data were also well correlated with the $Fe^{3+}/\Sigma Fe$ ratios, the correlation coefficients were slightly lower, i.e. $R^2 = 0.95$ and 0.87 for glasses and spinels, respectively. In contrast, the energy of the edge at a normalized height of 0.9 shows only poor correlation with the $Fe^{3+}/\Sigma Fe$ ratio of the spinels, especially for natural spinels (cf. Fig. EA6). Therefore, we used the pre-edge centroid as calibrated on the standards to determine the $Fe^{3+}/\Sigma Fe$-ratios of glasses and spinels present in the partial melting experiments.

In experiments where phases show strong differences in Fe contents, transmission images and edge-jump maps were sufficient for selecting individual minerals for the extraction of XANES spectra (Fig. 2f). In experiment groups "Re" and "AuPd1", PCA and *k*-means clustering maps (Fig. 2d) were needed to distinguish the spinels from the other phases, in particular from glass, because they have very similar bulk Fe contents. It was not possible to extract pure spinel spectra from samples of the "Graph" experimental series, mainly due to their small size (<5 μm), in comparison to the sample thickness (30 μm) and thus superimposition of the signal of surrounding phases (pyroxenes, olivine and glass) on the spinel signal.

Some glass spectra (e.g., for Re1-1370, Re1-1400 and Graph-1450) show slight differences in shape compared to the glass standards and, in particular, they have sharper Fe edges (Fig. EA4b, d). This is probably due to the presence of small quench crystals in the glass. For the sake of consistency, only the samples having comparable spectra to their corresponding standards (i.e. AuPd1 and AuPd2) were considered and used to determine $Fe^{3+}/\Sigma Fe$ ratios.

$Fe^{3+}/\Sigma Fe$ ratios of spinels and glasses from partial melting experiments determined from XANES pre-edge centroid values are reported in Table 6. For spinels, $Fe^{3+}/\Sigma Fe$ values on average range from 0.37 ± 0.08 for "Re1",

Table 5
$Fe^{3+}/\Sigma Fe$ ratio measured by Mossbauer, XANES centroid energy and alternative methods for $Fe^{3+}/\Sigma Fe$ determination for glass and spinel standards.

Standard name	ΔFMQ synthesis	$Fe^{3+}/\Sigma Fe$ Mössbauer	*2σ*	$Fe^{3+}/\Sigma Fe$ predicted[a]	Pre-edge centroid (eV)[b]	Energy at 0.9 norm. intensity (eV)[c]	XANES intensity ratios, $Fe^{3+}/\Sigma Fe$[d]
Glass SE1-3	−2	0.07	*0.04*	0.07	7111.744	7122.120	0.328
Glass SE1-4	−1.5	0.08	*0.04*	0.07	7111.742	7122.030	0.396
Glass SE1-2	−0.5	0.12	*0.04*	0.11	7111.870	7121.700	0.355
Glass SE1-1	1.5	0.29	*0.05*	0.23	7112.156	7122.510	0.413
Glass SE1-6	air	0.79	*0.04*	0.79	7113.215	7126.160	0.706
Dar8506-2		0.09	*0.01*	0.10	7111.709	7125.740	0.208
Mo8530-24		0.15	*0.02*	0.12	7111.724	7123.610	0.338
314-56		0.15	*0.02*	0.13	7111.798	7127.120	0.335
Mo-103		0.14	*0.01*	0.13	7111.798	7123.710	0.354
Mo79-1		0.17	*0.01*	0.16	7111.681	7124.150	0.320
8505-2		0.17	*0.03*	0.13	7111.789	7123.340	0.338
Dar8505-1		0.22	*0.01*	0.23	7111.829	7123.830	0.341
8506-3		0.22	*0.02*	0.25	7111.831	7126.290	0.346
Spi-Graph		0.50	*0.03*		7112.361	7125.550	0.483
Spi-Re		0.68	*0.04*		7112.595	7124.990	0.490
Spi-AuPd		0.77	*0.02*		7112.846	7126.410	0.578

[a] Fe^{3+}/Fe ratios calculated from ΔFMQ of synthesis using Kress and Carmichael (1991) for glasses and measured by Ionov and Wood (1992) for spinels.
[b] Pre-ege centroid calculated using pseudo-voigt functions as fitting model.
[c] Energy of the main absorbtion edge at 0.9 normalized Intensity (Berry et al., 2003, 2010).
[d] Intensity ratio determined by $I(Fe^{3+})/[I(Fe^{3+}) + I(Fe^{2+})]$ (Wilke et al., 2005)

Table 6
$Fe^{3+}/\Sigma Fe$ ratios of samples calculated from XANES centroid method, different models of fO_2 calculation and re-calculated $Fe^{3+}/\Sigma Fe$ ratios for glasses. Selected fO_2 and corresponding $Fe^{3+}/\Sigma Fe$ for glasses are highlighted in bold (see text for details).

Samples	$Fe^{3+}/\Sigma Fe$ Glasses measured by XANES	2σ	$Fe^{3+}/\Sigma Fe$ Spinels measured by XANES	2σ	$Fe^{3+}/\Sigma Fe$ Spinels calculated by stoichiometry	ΔQFM from glass-XANES[a]	2σ[b]	ΔQFM from spi-XANES[c]	2σ[b]	ΔQFM from spi -stoichiometry[d]	ΔQFM from Fe-alloy[e]	**selected ΔQFM[f]**	**2σ**	**Corrected $Fe^{3+}/\Sigma Fe$ for glasses[g]**	2σ	$Kd_{ol\text{-}liq}^{Mg-Fe^{2+}}$	2σ	$D_{Fe_2O_3}$ spinel−melt [h]	2σ	Bulk $D_{Fe_2O_3}$ peridotite−melt [i]	2σ
Graph-1370	0.17	*0.05*			0.23	0.2	*0.8*			−3.9	−3.0	**−3.5**	***0.6***	**0.04**	***0.01***	0.34	*0.01*				
Graph-1400	0.11	*0.04*			0.15	−1.4	*0.9*			−4.4	−3.2	**−3.8**	***0.8***	**0.04**	***0.01***	0.32	*0.01*				
Graph-1450					0.27					−3.1		**−3.1**	***0.7***	**0.04**	***0.01***	0.31	*0.02*				
Re1-1370					0.46					−1.7		**−1.7**	***0.4***	**0.08**	***0.03***	0.34	*0.02*				
Re1-1400			0.34	*0.08*	0.40			−1.8	*0.3*	−1.3	−0.7	**−1.3**	***0.5***	**0.10**	***0.04***	0.35	*0.02*	5.31	*1.25*	0.11	*0.03*
Re1-1440	0.22	*0.04*	0.39	*0.07*	0.47	1.1	*0.5*	−1.4	*0.2*	−1.0		**−1.2**	***0.3***	**0.10**	***0.02***	0.33	*0.01*	6.10	*1.11*	0.07	*0.03*
Re2-1440					0.47						−0.8	**−0.8**	***0.2***	**0.11**	***0.04***	0.33	*0.02*				
AuPd1-1310	0.33	*0.03*	0.58	*0.02*	0.54	2.3	*0.3*	−1.7	*0.1*	−1.6	−1.3	**−1.5**	***0.2***	**0.09**	***0.01***	0.28	*0.01*	10.76	*0.53*	0.26	*0.03*
AuPd1-1330	0.35	*0.03*	0.52	*0.05*	0.53	2.7	*0.3*	−2.1	*0.2*	−1.6	−0.5	**−1.4**	***0.8***	**0.09**	***0.05***	0.31	*0.02*	10.12	*0.51*	0.23	*0.03*
AuPd2-1320	0.70	*0.05*	0.98	*0.06*	0.89	5.6	*0.5*	2.0	*1.1*	3.4	−0.1	**5.6**	***0.6***	**0.70**	***0.05***	0.31	*0.05*	5.65	*0.35*	0.26	*0.01*
AuPd2-1330	0.77	*0.10*	0.97	*0.03*	0.86	6.4	*1.3*	1.8	*0.6*	3.0	0.0	**6.4**	***0.6***	**0.77**	***0.10***	0.45	*0.19*	4.88	*0.16*	0.19	*0.01*
AuPd2-1370	0.82	*0.09*	0.95	*0.05*	0.87	7.2	*1.5*	2.5	*0.5*	3.2	0.2	**7.2**	***0.7***	**0.82**	***0.09***	0.58	*0.30*	4.12	*0.22*	0.11	*0.01*

ΔQFM = fO_2 values relative to Quartz-Fayalite-Magnetite buffer.

[a] fO_2 calculated at 15 kbar from Kress and Carmichael (1991) model using XANES $Fe^{3+}/\Sigma Fe$ ratio for glasses. Uncertainites are soley based on the uncertainties of the XANES measurements.

[b] Uncertainites are soley based on the uncertainties of the XANES measurements.

[c] fO_2 calculated from spi-ol-opx oxygen barometry model from Mattioli and Wood (1988) using XANES $Fe^{3+}/\Sigma Fe$ ratio for spinels.

[d] Same model as [a] using $Fe^{3+}/\Sigma Fe$ ratio of spinels calculated by stochiometry.

[e] fO_2 calculated from Ir-Fe alloy following the method from Stagno and Frost (2010) for Re and Graph experiments, and from AuPd-Fe alloy using Barr and Grove (2010) model for AuPd experiments.

[f] selected fO_2 values using different models, see Section 5.1 for details.

[g] Corrected $Fe^{3+}/\Sigma Fe$ ratio of glasses using Kress and Carmichael (1991) model using selected fO_2 values, results from glass-XANES are used at the highest fO_2 (AuPd2 experiments).

[h] Ratio of Fe_2O_3 contents between spinel (C_{spi}) and glass (C_{gl}).

[i] Bulk partition coefficient (D) of Fe_2O_3 between minerals and melt, with Fe_2O_3 opx = 0.3, 0.8 wt% and Fe_2O_3 cpx = 0.4, 3 wt% for Re and AuPd1, AuPd2 respectively (Nimis et al., 2015).

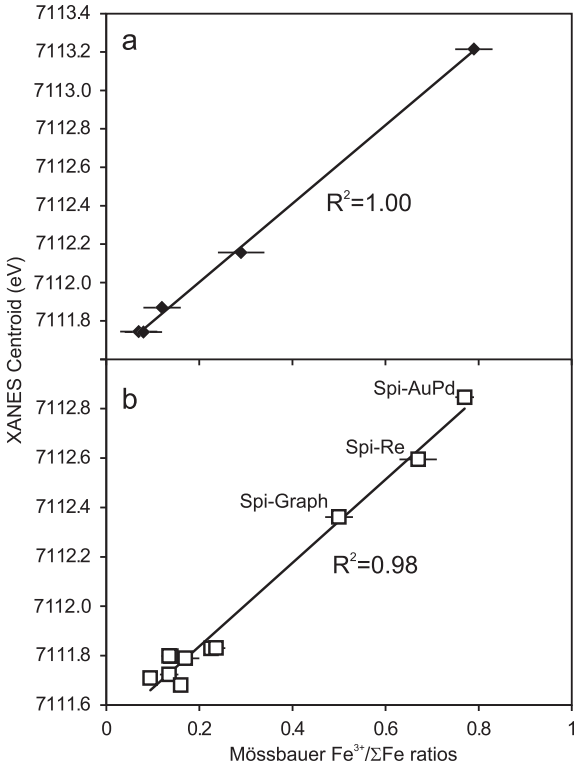

Fig. 5. Pre-edge centroids from XANES measurements as a function of $Fe^{3+}/\Sigma Fe$ obtained using Mössbauer spectroscopy for (a) glass standards, and (b) spinel standards. R^2 is the correlation coefficient.

0.55 ± 0.04 for "AuPd1" to 0.97 ± 0.05 for "AuPd2" samples and are in reasonable agreement with values calculated by stoichiometry, (generally within ± 0.1). $Fe^{3+}/\Sigma Fe$ ratios of glass samples vary from 0.14 ± 0.05 for "Graph" experiments, 0.22 ± 0.04 for "Re1", 0.34 ± 0.03 for "AuPd1" and 0.76 ± 0.1 for "AuPd2" experiments.

Assuming oxygen fugacities of the CCO buffer (i.e. $C + O_2 = CO_2$ or $\sim$ FMQ-3, e.g., Jakobsson and Oskarsson, 1994) for "Graph"-experiments and Re-ReO_2 buffer ($\sim$FMQ-1, Pownceby and O'Neill, 1994) for "Re"-experiments, expected glass $Fe^{3+}/\Sigma Fe$ ratios can be calculated using the calibration by Kress and Carmichael (1991). The glass $Fe^{3+}/\Sigma Fe$ ratios measured by XANES should be equal to or lower than the calculated values, because the fO_2 – buffers provide maximum values, due to the absence of CO_2-bubbles or ReO_2 in our experiments. However, with 0.14 ± 0.05 for "Graph" experiments and 0.22 ± 0.04 for "Re1" experiments, the XANES-measured glass $Fe^{3+}/\Sigma Fe$ ratios are more than twice the calculated values of 0.05 and 0.1, respectively. This might have a number of explanations. The deviation between the expected $Fe^{3+}/\Sigma Fe$ ratio based on the approximate fO_2 and that determined from the XANES measurements apparently increases with decreasing Fe_2O_3 content of the glasses. This may indicate that the number of glass standards was not sufficient to obtain suitable statistics at low Fe^{3+} concentrations. Consequently, in the following discussion other approaches have also been considered to estimate $Fe^{3+}/\Sigma Fe$ ratios of the glasses present in our experiments (see discussion 5.1).

5. DISCUSSION

5.1. Determination of oxygen fugacity

In order to determine the fO_2 of our experiments we tested four different model-approaches (Table 6). These include using the $Fe^{3+}/\Sigma Fe$ ratios of glasses measured by XANES ("glass-XANES"- Kress and Carmichael, 1991), using the $Fe^{3+}/\Sigma Fe$ ratios of spinels measured by XANES and those calculated by stoichiometry ("spi-XANES" and "spi-stoichiometry" – Mattioli and Wood, 1988) and using Fe-alloy sliding redox sensors ("Fe-alloy" – Woodland and O' Neill , 1997). The proportion of Fe that alloys with a noble metal in equilibrium with silicate assemblages is a function of the ambient oxygen fugacity (Woodland and O'Neill 1997). Ir was added to "Graph" and "Re" experiments so that Fe-Ir alloys were present in these experiments and fO_2 was determined using the method of Stagno and Frost (2010). AuPd-Fe alloy formed in AuPd experiments and fO_2 was calculated using the method of Barr and Grove (2010).

The comparison between fO_2 values obtained via the different models is illustrated in Fig. 6 and shows that all models have broadly comparable patterns: fO_2 "Graph" < fO_2 "AuPd1" < fO_2 "Re1" < fO_2 "AuPd2", "Graph" being the most reduced and AuPd2 the most oxidized experiments. The fO_2 values determined by the glass-XANES model, however, are approximately 2.5 log units higher than fO_2 values calculated from other models, as a result of extremely high $Fe^{3+}/\Sigma Fe$ ratios of glasses measured by XANES (cf. Section 4.2).

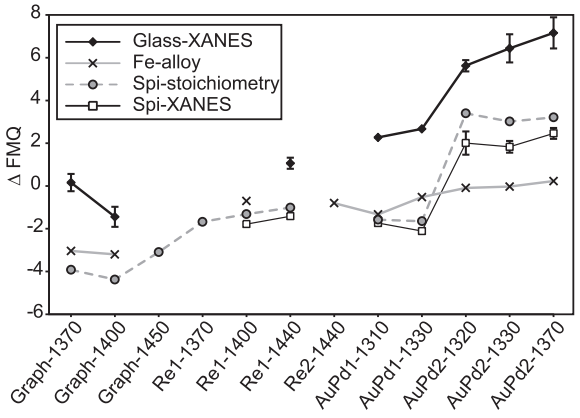

Fig. 6. A comparison between oxygen fugacity values, relative to the FMQ buffer, estimated using various methods for different experimental series. Details of these methods are reported in Section 5.1 and in the foot notes of Table 6. Uncertainties in fO_2 shown for the glass-XANES and spi-XANES methods are based on the uncertainties of the $Fe^{3+}/\Sigma Fe$ ratios determined by XANES only. Uncertainties in fO_2 from compositional uncertainties are typically 0.1–0.3 log-units for all oxybarometers (cf. Stagno and Frost, 2010).

For fO_2 conditions below FMQ (i.e. "Graph", "Re1" and "AuPd1" experiments), all models, except glass-XANES, are consistent and give values of approximately FMQ-3.3, FMQ-1.4 and FMQ-1.5, respectively. As previously mentioned, these values also agree with fO_2 values at the CCO and Re-ReO_2 buffers for "Graph" and "Re1" experiments. Above FMQ (i.e. "AuPd2" experiments) fO_2 values estimated from the Fe-alloy method (FMQ + 0.4) are lower than those calculated from spi-XANES or spi-stoichiometry models (FMQ + 2.7). However, under highly oxidizing conditions, such as those characterized by the "AuPd2" experiments, the proportion of Fe in the AuPd alloy is extremely low (≤0.3 wt%), which propagates to very large uncertainties in calculated fO_2. The Fe-alloy method is, therefore, not sufficiently accurate at conditions above FMQ. Moreover, spinels from "AuPd2" are at or very close to Fe^{3+}-saturation i.e. their $Fe^{3+}/\Sigma Fe$ ratios measured by XANES are close to 1. Therefore, it is very likely that the fO_2 calculated from the models using spinel as a oxybarometer (spi-XANES and spi-stoichiometry) are also inaccurate at such oxidizing conditions.

In summary, for the low fO_2 experiments (i.e. "Graph" series), glass $Fe^{3+}/\Sigma Fe$ ratios calculated from XANES data cannot be used for fO_2 calculations. Furthermore, spinel grains synthesized at these conditions were too small to be analysed by XANES. However, spinel $Fe^{3+}/\Sigma Fe$ ratios and fO_2 calculations using spinel stoichiometry and Fe-alloy values are consistent, and also match expected values for CCO-buffered conditions. For intermediate fO_2 experiments ("Re" and "AuPd1"), all models used to determine fO_2 are consistent, except that based on glass-XANES measurements. For high fO_2 experiments ("AuPd2"), it would appear that the fO_2 can be calculated reliably from Fe^{3+}/Fe^{2+} ratio measurements by XANES. Centroid values of "AuPd2" are similar to those calculated for standard glass SE1-FE6 (~7113.2 ± 0.3), implying that their $Fe^{3+}/\Sigma Fe$ ratios (~0.8–0.9) as well as their relative fO_2 are comparable as highlighted by the glass-XANES model. In contrast fO_2 determination using spi-XANES, spi-stoichiometry or Fe-alloy models are not suitable for such highly oxidizing conditions.

According to these criteria, the most reliable fO_2 estimates were selected for each sample series (Table 6). For "Graph" experiments (FMQ-3.5) this corresponded to the average fO_2 values determined using spinel stoichiometry and Fe-alloy models. For "AuPd-1" (FMQ-1.5) and "Re1" (FMQ-1.4) experiments averages of fO_2 determined from spinel stoichiometry, Fe-alloy and spinel-XANES measurements were used. Oxygen fugacities determined from the Fe-alloy redox sensor were used for "Re2" experiments (FMQ-0.8), whereas fO_2 estimates based on the glass-XANES measurements were used for "AuPd2" experiments (FMQ + 6.2). The uncertainties arising from compiling fO_2 values from different methods can be evaluated from the propagated uncertainties on the re-calculated fO_2 (Table 6). For those experiments where several models have been averaged to generate the re-calculated fO_2, the 2-sigma uncertainty is between 0.2 and 0.8 log-units. Compiled uncertainties are higher than the uncertainties on one single fO_2 sensor, which are typically propagated solely from compositional uncertainties and are on the order of 0.2–0.3 log-units (e.g. Stagno and Frost, 2010). We attribute the differences between the fO_2 sensors to the lack of internal consistency in the required thermodynamic data, implying that the use of a single fO_2 sensor may not yield reliable results in complex systems or at least may lead to underestimated real uncertainties. Comparing different methods thus provides more realistic, albeit larger, uncertainties on fO_2 estimated in high-pressure experiments. Using the selected values of fO_2 for the experimental series, $Fe^{3+}/\Sigma Fe$ ratios of glasses were then calculated for the "Graph", "Re1", "Re2" and "AuPd1" experiments using the model of Kress and Carmichael (1991), which yields average ratios of 0.04, 0.10, 0.11 and 0.09, respectively. The accuracy of the corrected melt $Fe^{3+}/\Sigma Fe$ ratios, was tested by performing two sandwich-experiments run at the same conditions as the partial melting experiments "Graph-1400" and "Re2-1370" (see Section 2.2). Oxygen fugacities calculated from the $Fe^{3+}/\Sigma Fe$ ratios of the glass layers using the Kress and Carmichael (1991) model are FMQ-2.8 for "S-Graph" and FMQ-0.8 for "S-Re2" and are in near-perfect agreement with oxygen fugacitites determined from the analysis of the Fe-Ir alloy present in these experiments (FMQ-3 and FMQ-0.7 - Stagno and Frost, 2010). As will be discussed in the next section, the melts contain variable amounts of H_2O, hence, the relationship between fO_2 and $Fe^{3+}/\Sigma Fe$ determined for dry conditions by Kress and Carmichael (1991) appears to be also valid for H_2O-bearing systems. The $Fe^{3+}/\Sigma Fe$ and fO_2 values of the sandwich experiments are also in excellent agreement with values estimated for the "Graph" and "Re2" partial melting experiments, thus demonstrating the consistency of the corrected $Fe^{3+}/\Sigma Fe$ ratios of the glasses (Fig. 7).

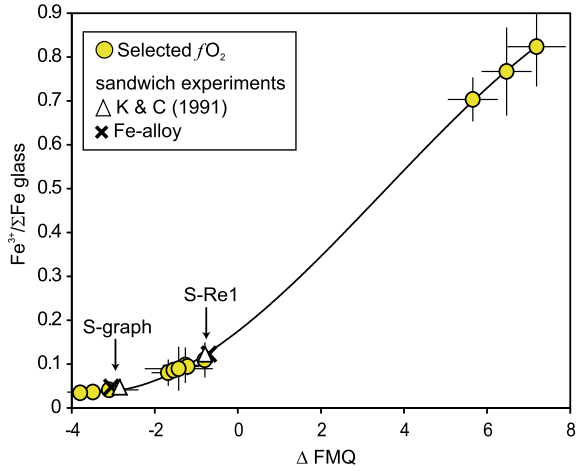

Fig. 7. $Fe^{3+}/\Sigma Fe$ ratios of glasses re-calculated using the Kress and Carmichael (1991) model from the "selected" fO_2 values (cf. Section 5.1 for details) *vs.* ΔFMQ. Measurements of glasses from additional sandwich experiments (S-graph and S-Re1) are also shown. The $Fe^{3+}/\Sigma Fe$ ratios of these glasses were measured by Mössbauer spectroscopy and their fO_2 values were determined using both an Fe-alloy sliding redox sensor and the Kress and Carmichael (1991) model based on the glass $Fe^{3+}/\Sigma Fe$ ratio. (For interpretation of the references to color in this figure legend, the reader is referred to the web version of this article.)

These new ratios were also used to calculate the Fe^{2+}-Mg exchange coefficient between olivine and liquid (i.e., $Kd_{Ol-liq}^{Mg-Fe^{2+}}$) for each of the experiments. The majority of calculated *Kd* values range from 0.28 ± 0.01 to 0.35 ± 0.02 (Table 6) and agree within error with proposed equilibrium values calculated using the model of Toplis (2005) for the specific conditions. Two of the most oxidizing experiments show significantly higher *Kd* of 0.45 ± 0.19 and 0.58 ± 0.3, but are still within error of the proposed equilibrium values. Calculated values for *Kd* are highly sensitive to the $Fe^{3+}/\Sigma Fe$ of the glasses, explaining the high values and uncertainties.

5.2. Effect of water and Fe^{3+} on melting reactions and melt productivity

Despite efforts to maintain dry conditions in the experiments, FTIR analyses revealed the presence of H_2O in experimental glasses, similar to previous experimental studies (e.g. Green et al., 2014; Rosenthal et al., 2014). Glasses from "Graph" samples show the lowest H_2O contents of 0.05–0.16 wt%, a glass from "Re2" experiments contained 0.44 wt%, and the highest values of 0.69–0.85 wt% were measured for glasses from both "AuPd" series (Table 2). The H_2O concentration of the glasses overall increases with increasing $Fe^{3+}/\Sigma Fe$ ratio of the glass and thereby fO_2 (e.g. Berndt et al., 2002 – Fig. 8a). Thus, water is likely incorporated during the experiment as a result of hydrogen diffusion through the metallic capsule, which then forms H_2O by reducing iron in the peridotite following the reaction (e.g. Gaillard et al., 2003):

$$2H + Fe_2O_3 \rightarrow H_2O + 2FeO \quad (1)$$

The experiments with the most oxidized starting material thus have the highest potential to reduce H_2 and to dissolve water in the melts. We estimated bulk H_2O contents of the samples, assuming that H_2O behaves perfectly incompatibly during melting and was thus quantitatively partitioned into the silicate melt. Similar to glass H_2O contents, bulk H_2O contents also increase with fO_2 (Fig. 8b). Exceptions are the "Re2" experiments that show the highest bulk H_2O contents of 0.19 wt% H_2O at FMQ-0.8. As expected from previous studies (e.g. Foley, 2011), partial melting degree and melt productivity (dF/dT) increase with increasing bulk H_2O content of the samples (Fig. 9), but there is no clear correlation with fO_2. Our experiments do not show any effect that can be clearly assigned to that of Fe^{3+} on melt productivity. If high $Fe^{3+}/\Sigma Fe$ would lead to increased melt productivity, this effect should be most visible in the most oxidized AuPd2 experiments (FMQ + 6.3). The fO_2 of these experiments is more than 7 log-units higher than the fO_2 of the other experiments, but they closely follow the trend of increasing dF/dT as a function of bulk H_2O (Fig. 9). Any additional effect arising from Fe^{3+} on melt productivity would therefore appear to be relatively minor compared to that of H_2O and will not be significant for natural systems that are almost never completely dry.

The presence of H_2O in experiments has a direct effect on the melting reactions that can be gauged by examining the mineral modes as a function of F (cf. Table EA2). For "Graph" experiments, olivine, clinopyroxene and spinel react to produce orthopyroxene and liquid. Overall,

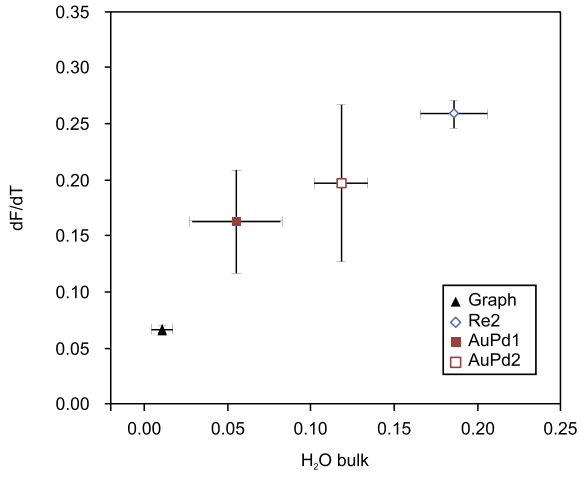

Fig. 9. Melt productivity (dF/dT) as a function of bulk water content for the various experimental series.

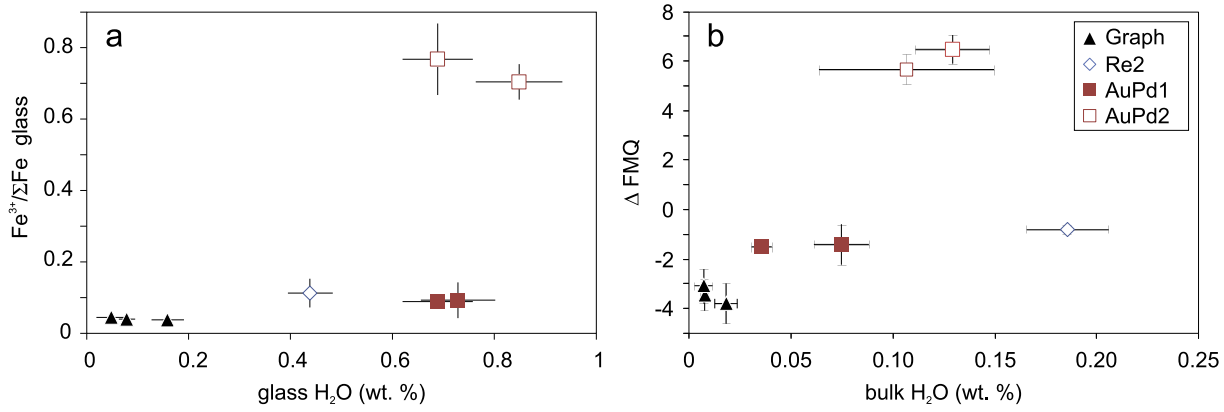

Fig. 8. (a) $Fe^{3+}/\Sigma Fe$ ratios of the glasses as a function of glass H_2O contents (b) Selected fO_2 (expressed as ΔFMQ) of the experiments as a function of bulk H_2O contents.

for "Re" and "AuPd" experiments orthopyroxene and clinopyroxene are consumed to create olivine and liquid. The proportion of olivine formed is positively correlated to the H_2O content of the coexisting melts, implying that H_2O causes the stability field of olivine to expand relative to that of orthopyroxene (e.g., Kushiro, 1969, 1972). A detailed summary of the melting reactions can be found in the electronic annex (Table EA2).

5.3. Mineral-melt Fe_2O_3 partitioning from experiments and modelling

Partition coefficients between residual minerals and melt are required to model the behaviour of Fe_2O_3 during partial melting of the mantle. We combined the total Fe-content of spinels and glasses (analysed as FeO_{total} by EPMA) with their $Fe^{3+}/\Sigma Fe$ ratios (XANES for spinels, see Section 5.1 for glasses) to calculate Fe_2O_3 concentration in both phases and its spinel-melt partition coefficient ($D^{spinel-melt}_{Fe_2O_3}$). As shown in Fig. 10a, our experiments show a distinct drop in $D^{spinel-melt}_{Fe_2O_3}$ from AuPd1-experiments to Re1 experiments at low fO_2 conditions (~FMQ-1.5), whereas $D^{spinel-melt}_{Fe_2O_3}$ is the same within error for Re1 and AuPd2 experiments up to FMQ + 6 (Table 6). As there are insufficient data points to draw strong conclusions concerning why the partition coefficients evolve in this way, we have compared our data to results from a batch-melting model using pMELTS (Ghiorso et al., 2002). Thermodynamic modelling using pMELTs can be empolyed as an independent tool to examine the relative behaviour of Fe^{3+} and Fe^{2+} during partial melting. To facilitate direct comparison to our experiments, we assumed a MPY-90 composition with initial bulk $Fe^{3+}/\Sigma Fe$ ratios ranging from 0.01 to 0.8. The compositions of both melt and minerals were calculated at 1.5 GPa and temperatures between 1320 and 1500 °C. Using these model-results, $D^{spinel-melt}_{Fe_2O_3}$ were obtained and fO_2 was calculated at each step using the spinel-peridotite oxybarometer from Mattioli and Wood (1988). Indeed, the pMELTS model with the lowest bulk $Fe^{3+}/\Sigma Fe$ ratio predicts a sharp increase in $D^{spinel-melt}_{Fe_2O_3}$ at low fO_2, similar to our experimental results (Fig. 10a). From this comparison an estimate can be made of the approximate bulk $Fe^{3+}/\Sigma Fe$ in the different experimental charges, i.e., about 0.8 for AuPd2, 0.05–0.1 for AuPd1 and Re1.

Bulk Fe_2O_3 partition coefficients ($D^{peridotite-melt}_{Fe_2O_3}$) were then estimated using the mineral proportions of those experiments for which $Fe^{3+}/\Sigma Fe$ ratios of spinels could be determined. Estimates for the Fe_2O_3 contents of orthopyroxene and clinopyroxene as a function of fO_2 are based on values measured by Nimis et al. (2015) on natural samples. These Fe_2O_3 contents range from 0.2 to 0.8 wt% for orthopyroxene and from 0.3 to 3 wt% for clinopyroxene, depending on fO_2. Note that the minor proportion of Fe^{3+} in olivine does not have a significant effect on the bulk partition coefficient. The resulting bulk $D^{peridotite-melt}_{Fe_2O_3}$ values for the experiments vary from 0.09 for Re1, 0.24 for "AuPd1" and 0.19 for "AuPd2", and are not obviously correlated with fO_2 (Table 6), contrary to the modelling results presented by Gaetani (2016). Nevertheless, both studies call for non-constant $D^{peridotite-melt}_{Fe_2O_3}$ during partial melting.

In detail, some differences can be seen as to which minerals control Fe_2O_3. At low fO_2 (~FMQ-1.5) bulk $D^{peridotite-melt}_{Fe_2O_3}$ is controlled by decreasing amounts of residual orthopyroxene and clinopyroxene ("AuPd1" experiments - Fig. EA7 in the Electronic Annex), for both of which $D^{mineral-melt}_{Fe_2O_3}$ decrease with ongoing melting. Towards high degrees of partial melting, orthopyroxene governs the partitioning of Fe_2O_3, as clinopyroxene is exhausted from the residual mineral assemblage ("Re1" experiments). Under oxidizing conditions (~FMQ + 6.2, "AuPd2" experiments- Fig. EA7) the partitioning of Fe_2O_3 is dominated by the larger fraction of residual spinel due to its high Fe_2O_3 concentrations (~5 wt% spinel occurs in the residual mineral assemblage which contains up to 50 wt% FeO_{total} and has an $Fe^{3+}/\Sigma Fe$ ratio close to 1). $D^{spinel-melt}_{Fe_2O_3}$ decreases

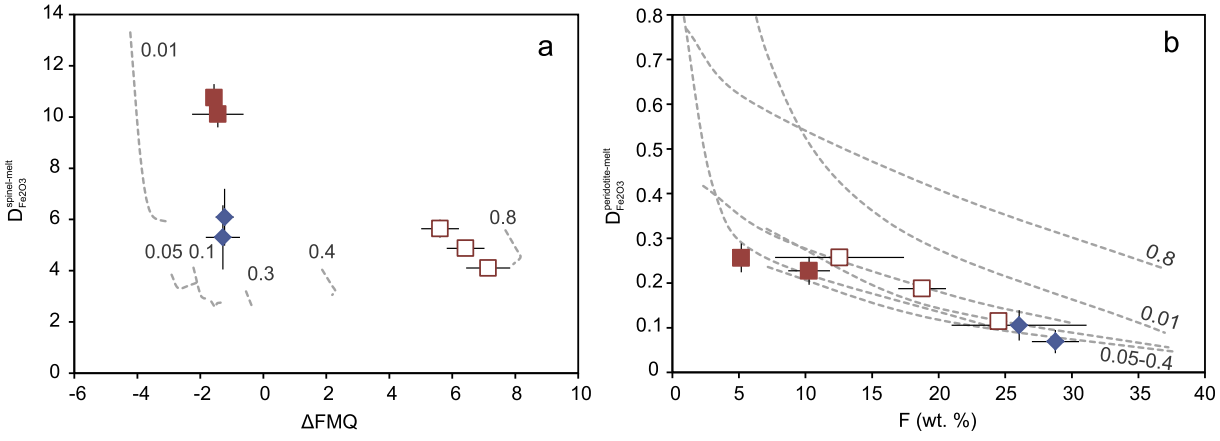

Fig. 10. Experimentally determined mineral/melt partition coefficients for Fe_2O_3 compared with values determined using pMELTS calculations (dashed curves) for partial melting of MPY-90 at 1.5 GPa. Bulk $Fe^{3+}/\Sigma Fe$ ratios for model calculations range from 0.01 to 0.8 (numbers next to the curves). (a) $D^{spinel-melt}_{Fe_2O_3}$ as a function of fO_2 (ΔFMQ). (b) The bulk $D^{peridotite-melt}_{Fe_2O_3}$ as a function of partial melting degree (F in wt%).

with increasing melt fraction, and so does bulk $D^{peridotite-melt}_{Fe_2O_3}$. The overall effect is such that $D^{peridotite-melt}_{Fe_2O_3}$ decreases with increasing degree of partial melting, regardless of fO_2 (Fig. 10b). This shows that Fe_2O_3 is less incompatible at lower degrees of melting than at higher degrees. This correlation is also well supported by the results of pMELTS calculations, as highlighted in Fig. 10b. Varying $D^{peridotite-melt}_{Fe_2O_3}$ during partial melting was also invoked by Gaetani (2016) based on a model using point defect thermodynamics.

5.4. Implications for the behaviour of Fe_2O_3 during MORB genesis

As outlined in the introduction, there appears to be no correlation in global MORB analyses between $Fe^{3+}/\Sigma Fe$ of the glasses and parameters sensitive to the degree of partial melting such as $Na_2O_{(8)}$ (Bézos and Humler, 2005; Cottrell and Kelley, 2011). However, if Fe_2O_3 is mildly incompatible during partial melting (e.g. Canil et al., 1994), $Fe^{3+}/\Sigma Fe$ ratios of partial melts should decrease as the degree of partial melting increases. Hence, a positive correlation between $Fe^{3+}/\Sigma Fe$ and other incompatible elements such as Na_2O or TiO_2 would be expected, but is not observed. Our results offer a possible solution to this issue. If the bulk partition coefficient for Fe_2O_3 indeed decreases as the melting degree increases as described in the previous section, then there will be a tendency for the rock to retain more Fe_2O_3 at lower melting degrees. The decrease in bulk $D^{peridotite-melt}_{Fe_2O_3}$ can then counterbalance the expected decrease in melt $Fe^{3+}/\Sigma Fe$ ratio with higher degrees of melting and the net result is that $Fe^{3+}/\Sigma Fe$ ratios of the partial melts remain relatively constant over a range of melting degrees.

This effect is illustrated in Fig. 11 where melt $Fe^{3+}/\Sigma Fe$ ratios of our experimental glasses are plotted as a function of melt Na_2O for our experiments and are compared with calculations employing pMELTS. Our experimental results are consistent with pMELTS calculations, considering the initial bulk $Fe^{3+}/\Sigma Fe$ ratios of the experiments (i.e., ~0.8 for AuPd2, 0.05–0.1 for "AuPd1" and "Re1" – see Section 5.3). Global MORB analyses are also shown, demonstrating the narrow and almost constant melt $Fe^{3+}/\Sigma Fe$ ratio of ~0.12 (i.e. ~ FMQ), while Na_2O changes significantly. Similarly, the $Fe^{3+}/\Sigma Fe$ ratios of our experimental glasses and those predicted from the pMELTS calculations for melting degrees between 1 and 37% also remain constant through this melting interval. This comparison demonstrates that the absence of correlation between MORB and partial melting indicators could be explained through the behaviour of Fe_2O_3 during mantle source melting, i.e. the combined effect of Fe_2O_3 being mildly incompatible combined with the observed decrease in bulk $D^{peridotite-melt}_{Fe_2O_3}$ with increasing degree of partial melting.

The fO_2 of MORB genesis is clearly higher than that of the "Graph" experiments (~FMQ-3.5), indicating that graphite cannot be present during MORB genesis to buffer the $Fe^{3+}/\Sigma Fe$ ratio as was proposed by Kadik (1997) and

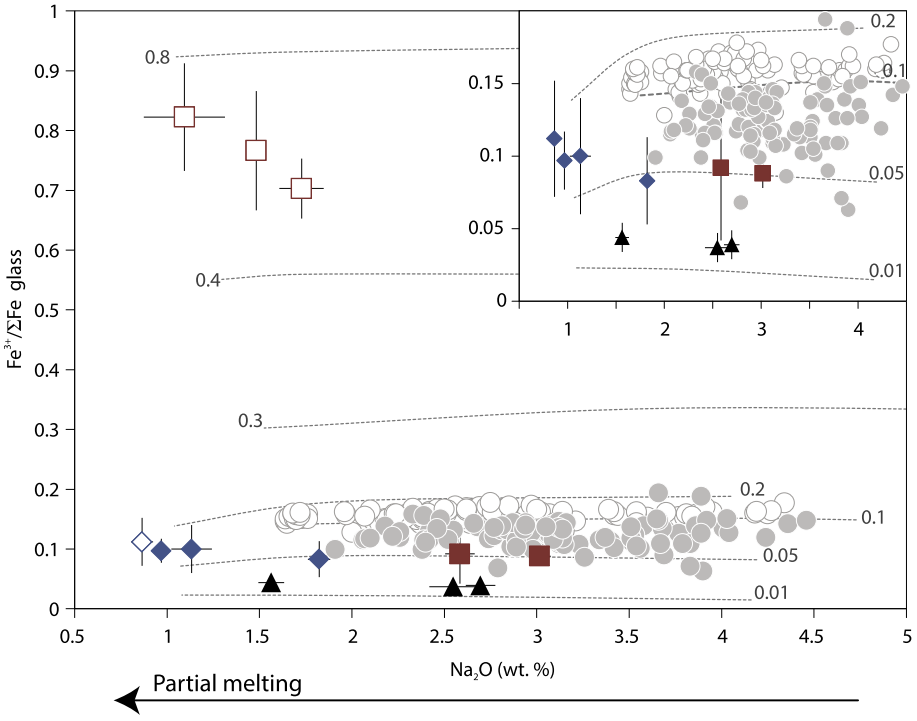

Fig. 11. $Fe^{3+}/\Sigma Fe$ ratio versus Na_2O content of experimental glasses compared with predictions from pMELTS modelling (dotted curves) of partial melts formed from MPY-90 at 1.5 GPa with initial $Fe^{3+}/\Sigma Fe$ ratios ranging from 0.01 to 0.8 (numbers next to the curves). Primitive MORB glass analyses from Bézos and Humler (2005) (filled grey circles) and from Cottrell and Kelley (2011) (empty grey circles) are shown for comparison. The arrow indicates the direction of Na_2O content evolution with increasing degree of partial melting.

Holloway (1998). In contrast, MORB have $Fe^{3+}/\Sigma Fe$ ratios corresponding to fO_2 values of around FMQ, which is about 1 to 1.5 log units above those of the "AuPd1" and "Re1" experiments (~FMQ-1.5 to -1.2). pMELTS modelling indicates that the range of global MORB glasses originate from a mantle source containing between 0.1 and 0.5 wt% Fe_2O_3. The lowest values (i.e., between 0.1 and 0.3 wt % Fe_2O_3) are in agreement with the Fe_2O_3 contents measured for natural spinel peridotites (Canil and O'Neill, 1996; Woodland et al., 2006; Frost and McCammon, 2008). The values above 0.3 wt% Fe_2O_3 might simply imply a mantle source more fertile and consequently with a larger Fe_2O_3 content than lithospheric samples, but they could also imply the presence of heterogeneities in the MORB mantle source, such as websterite or pyroxenite rocks that have raised bulk Fe_2O_3 contents (Canil and O'Neill, 1996).

6. SUMMARY AND CONCLUSIONS

We have performed partial melting experiments on a MORB mantle source at 1.5 GPa, under variable fO_2 conditions (FMQ-3.5 to FMQ + 6), using different capsule materials (graphite, Re, AuPd) and initial starting material oxidation states. XANES data collected in full-field mode were used to determine $Fe^{3+}/\Sigma Fe$ ratios of spinels in the experimental charges but the analytical conditions used in this study were not suitable for $Fe^{3+}/\Sigma Fe$ quantification of the resulting glasses. Experimental oxygen fugacities and $Fe^{3+}/\Sigma Fe$ ratios of glasses were consequently determined from a combination of thermodynamic modelling and iron-alloy sliding redox sensors. These estimates were then validated using a new set of peridotite-basalt sandwich experiments that yielded glass portions of sufficient size for Mössbauer spectroscopy measurements. The presence of H_2O detected in the glasses is responsible for changes in the melting reactions; in particular, it increases the stability field of olivine. pMELTS modelling of the partial melting of a peridotite at variable fO_2 conditions are consistent with our experimental data, which provides an important improvement in our understanding of the behaviour of Fe_2O_3 during MORB genesis. We demonstrate that the bulk $D_{Fe_2O_3}^{peridotite-melt}$ decreases with increasing partial melting degree, which causes melt $Fe^{3+}/\Sigma Fe$ ratios to remain constant over varying degrees of partial melting. Accordingly, we argue that this behaviour is sufficient to explain the apparent absence of a correlation between $Fe^{3+}/\Sigma Fe$ ratios of global primitive MORB glasses and indices of partial melting degree.

ACKNOWLEDGEMENTS

We would like to thank Hubert Schulze and Raphael Njul for sample preparation, Detlef Krauße for his assistance with EPMA work as well as the members of the mechanical and electronics workshops at BGI for their invaluable help. Dimitri Ionov is thanked for providing spinel samples used as standards for XANES as well as A. Mallik and E. S. Jennings for discussions. The manuscript greatly benefited from constructive comments by Dante Canil, Fabrice Gaillard and an anonymous reviewer, as well as by Associate Editor Mike Toplis. We acknowledge the European Synchrotron Radiation Facility for provision of synchrotron radiation facilities. The project was funded through a research fellowship by the Alexander von Humboldt Foundation to F.S. V.L. was supported by the European Research Council Advanced Grant 'ACCRETE' (contract number 290568) and A.R. was supported by European Research Council Marie-Curie International Incoming Fellowship (contract number 302637). D.F recognises grant number I-1239-301.8/2014 of the German Israeli Foundation.

REFERENCES

Albarede F. and Provost A. (1977) Petrological and geochemical mass-balance equations- an algorithm for least-square fitting and general error analysis. *Comput. Geosci.* **3**, 309–326.

Alberto H. V., Pinto da Cunha J. L., Mysen B. O., Gil J. M. and Ayres de Campos N. (1996) Analysis of Mössbauer spectra of silicate glasses using a two-dimensional Gaussian distribution of hyperfine parameters. *J. Non-Cryst. Solids* **194**, 48–57.

Ballhaus C., Berry R. F. and Green D. H. (1991) High pressure experimental calibration of the olivine-orthopyroxene-spinel oxygen geobarometer: implications for the oxidation state of the upper mantle. *Contrib. Mineral. Petrol.* **107**, 27–40.

Barr J. and Grove T. L. (2010) AuPdFe ternary solution model and applications to understanding the fO_2 of hydrous, high pressure experiments. *Contrib. Mineral. Petrol.* **160**, 631–643.

Berndt J., Liebske C., Holtz F., Freise M., Nowak M., Ziegenbein D., Hurkuck W. and Koepke J. (2002Barr) A combined rapid quench and H_2-membrane setup for internally heated pressure vessels: description and application for water solubility in basaltic melts. *Am. Mineral.* **87**, 1717–1726.

Berry A. J., O'Neill H. St. C., Jayasuriya K. D., Campbell S. J. and Foran G. J. (2003) XANES calibrations for the oxidation state of iron in a silicate glass. *Am. Mineral.* **88**, 967–977.

Berry A. J., Danyushevsky L. V., O'Neill H., St C., Newville M. and Sutton S. R. (2008) The oxidation state of iron in komatiitic melt inclusions indicates hot Archaean mantle. *Nature* **455**, 961–963.

Berry A. J., Yaxley G. M., Woodland A. B. and Foran G. J. (2010) A XANES calibration for determining the oxidation state of iron in mantle garnet. *Chem. Geol.* **278**, 31–37.

Bézos A. and Humler E. (2005) The $Fe^{3+}/\sum Fe$ ratios of MORB glasses and their implications for mantle melting. *Geochim. Cosmochim. Acta* **69**, 711–725.

Borisov A., Palme H. and Spettel B. (1994) Solubility of Pd in silicate melts: implications for core formation in the Earth. *Geochim. Cosmochim. Acta* **58**, 705–716.

Borisov A. and Jones J. H. (1999) An evaluation of Re, as an alternative to Pt, for the 1 bar loop technique: An experimental study at 1400°C. *Am. Mineral.* **84**, 1528–1534.

Canil D., O'Neill H., St C., Pearson D. G., Rudnick R. L., McDonough W. F. and Carswell D. A. (1994) Ferric iron in peridotites and mantle oxidation states. *Earth Planet. Sci. Lett.* **123**, 205–220.

Canil D. and O'Neill H. St. C. (1996) Distribution of ferric iron in some upper-mantle assemblages. *J. Petrol.* **37**, 609–635.

Canil D. (2002) Vanadium in peridotites, mantle redox and tectonic environments: Archean to present. *Earth Planet. Sci. Lett.* **195**, 75–90.

Canil D., Johnston S. T. and Mihalynuk M. (2006) Mantle redox in Cordilleran ophiolites as a record of oxygen fugacity during partial melting and the lifetime of mantle lithosphere. *Earth Planet. Sci. Lett.* **248**, 106–117.

Carmichael I. S. E. (1991) The redox states of basic and silicic magmas: a reflection of their source regions? *Contrib. Mineral. Petrol.* **106**, 129–141.

Chase M. W. (1998) NIST-JANAF Themochemical Tables, Fourth Edition. *J. Phys. Chem. Ref. Data, Monogr.* **9**, 1–1951.

Cottrell E. and Kelley K. A. (2011) The oxidation state of Fe in MORB glasses and the oxygen fugacity of the upper mantle. *Earth Planet. Sci. Lett.* **305**, 270–282.

Davis F. A., Cottrell E., Birner S. K., Warren J. M. and Lopez O. G. (2017) Revisiting the electron microprobe method of spinel-olivine-orthopyroxene oxybarometry applied to spinel peridotites. *Am. Mineral.* **102**, 421–435.

De Andrade V., Susini J., Salome M., Beraldin O., Rigault C., Heymes T., Lewin E. and Vidal O. (2011) Submicrometer hyperspectral X-ray imaging of heterogeneous rocks and geomaterials: Applications at the Fe *K*-edge. *Anal. Chem.* **83**, 4220–4227.

Falloon T. J. and Green D. H. (1987) Anhydrous partial melting of MORB pyrolite and other peridotite compositions at 10 kb: Implications for the origin of primitive MORB glasses. *Contrib. Mineral. Petrol.* **37**, 181–219.

Fayard B., Pouyet E., Berruyer G., Bugnazet D., Cornu C., Cotte M., De Andrade V., Di Chiaro F., Hignette O., Kieffer J., Martin T., Papillon E., Salomé M. and Solé V. A. (2013) The new ID21 XANES full-field end-station at ESRF. *J. Phys.: Conf. Ser.* **425**. https://doi.org/10.1088/1742-6596/425/19/192001.

Foley S. F. (2011) A reappraisal of redox melting in the Earth's mantle as a function of tectonic setting and time. *J. Petrol.* **52**, 1363–1391.

Frost D. J. and McCammon C. A. (2008) The redox state of Earth's mantle. *Annu. Rev. Earth Planet. Sci.* **36**, 389–420.

Gaetani G. A. (2016) The behaviour of $Fe^{3+}/\Sigma Fe$ during partial melting of spinel lherzolite. *Geochim. Cosmochim. Acta* **185**, 64–77.

Gaillard F., Pichavant M., Mackwell S., Champallier R., Scaillet B. and McCammon C. (2003) Chemical transfer during redox exchanges between H_2 and Fe-bearing silicate melts. *Am. Mineral.* **88**, 308–315.

Gaillard F., Scaillet B., Pichavant M. and Iacono-Marziano G. (2015) The redox geodynamics linking basalts and their mantle sources through space and time. *Chem. Geol.* **418**, 217–233.

Ghiorso M. S., Hirschmann M. M., Reiners P. W. and Kress V. C. (2002) The pMELTS: A revision of MELTS for improved calculation of phase relations and major element partitioning related to partial melting of the mantle to 3 GPa. *Geochem. Geophy. Geosy.* **3**. https://doi.org/10.1029/2001GC000217.

Green D. H. and Falloon T. J. (1998) Pyrolite: A ringwood concept and its current expression. In *The Earth's Mantle* (ed. I. Jackson). Cambridge University Press, Cambridge, pp. 311–378.

Green D. H., Falloon T. J., Eggins S. M. and Yaxley G. M. (2001) Primary magmas and mantle temperatures. *Eur. J. Mineral.* **13**, 437–451.

Green D. H. and Falloon T. J. (2005) Primary magmas at mid-ocean ridges, "hotspots", and other intraplate settings: constraints on mantle potential temperature. In: Foulger G. R., Natland J. H., Presnall D. C., Anderson D. L. (Eds.), Plates, Plumes, and Paradigms: Geological Society of America Special Paper, vol. 388, pp. 217–247.

Gonzalez-Jimenez I. D., Cats K., Davidian T., Ruitenbeek M., Meirer F., Liu Y., Nelson J., Andrews J. C., Pianetta P., de Groot F. M. F. and Weckhuysen B. M. (2012) Hard X-ray nanotomography of catalytic solids at work. *Angew. Chem. Int. Edit.* **51**, 11986–11990.

Hirschmann M. M. (2012) Magma ocean influence on early atmosphere mass and composition. *Earth Planet. Sci. Lett.* **341**, 48–57.

Holloway J. R. and Burnham C. W. (1972) Melting relations of basalt with equilibrium water pressure less than total pressure. *J. Petrol.* **13**, 1–29.

Holloway J. R. (1998) Graphite-melt equilibria during partial melting: constraints on CO_2 in MORB magmas and the carbon content of the mantle. *Chem. Geol.* **147**, 89–97.

Ionov D. A. and Wood B. J. (1992) The oxidation state of subcontinental mantle: oxygen thermobarometry of mantle xenoliths from central Asia. *Contrib. Mineral. Petrol.* **111**, 179–193.

Jakobsson S. and Oskarsson N. (1994) The system C-O in equilibrium with graphite at high pressure and temperature: An experimental study. *Geochim. Cosmochim. Acta* **58**, 9–17.

Kadik A. (1997) Evolution of Earth's redox state during upwelling of carbon-bearing mantle. *Phys. Earth Planet. Int.* **100**, 157–166.

Kasting J. F., Eggler D. H. and Raeburn S. P. (1993) Mantle redox evolution and the oxidation state of the Archean atmosphere. *J. Geol.* **101**, 245–257.

Klein E. M. and Langmuir C. H. (1987) Global correlations of ocean ridge basalt chemistry with axial depth and crustal thickness. *J. Geophys. Res.* **92**, 8089–8115.

Kress V. C. and Carmichael I. S. E. (1991) The compressibility of silicate liquids containing Fe_2O_3 and the effect of composition, temperature, oxygen fugacity and pressure on their redox states. *Contrib. Miner. Petrol.* **108**, 82–92.

Kushiro I. (1969) The system forsterite-diopside-silica with and without water at high pressures. *Am. J. Sci.* **267A**, 269–294.

Kushiro I. (1972) Effect of water on the composition of magmas formed at high pressures. *J. Petrol.* **13**, 311–334.

Lagarec K. and Rancourt D. G. (1997) Extended Voigt-based analytic lineshape method for determining N-dimensional correlated hyperfine parameter distributions in Mössbauer spectroscopy. *Nucl. Instrum. Methods Phys. Res. Sect. B* **129**, 266–280.

Laporte D., Toplis M., Seyler M. and Devidal J.-L. (2004) A new experimental technique for extracting liquids from peridotite at very low degrees of melting: Application to partial melting of depleted peridotite. *Contrib. Mineral. Petrol.* **146**, 463–484.

Laurenz V., Fonseca R. O. C., Ballhaus C. and Sylvester P. J. (2010) Solubility of palladium in picritic melts: 1. The effect of iron. *Geochim. Cosmochim. Acta* **74**, 2989–2998.

Lécuyer C. and Ricard Y. (1999) Long-term fluxes and budget of ferric iron: implication for the redox states of the Earth's mantle and atmosphere. *Earth Planet. Sci. Lett.* **165**, 197–211.

Lee C.-T. A., Luffi P., Plank T., Dalton H. and Leeman W. P. (2009) Constraints on the depths and temperatures of basaltic magma generation on Earth and other terrestrial planets using new thermobarometers for mafic magmas. *Earth Planet. Sci. Lett.* **279**, 20–33.

Liu Y., Meirer F., Williams P. A., Wang J., Andrews J. C. and Pianetta P. (2012) TXM-Wizard: a program for advanced data collection and evaluation in full-field transmission X-ray microscopy. *J. Synchrotron Radiat.* **19**, 281–287.

Mackwell S. (2008) Rheological consequences of redox state. *Rev. Miner. Geochem.* **68**, 555–569.

Mallmann G. and O'Neill H. St. C. (2009) The crystal/melt partitioning of V during mantle melting as a function of oxygen fugacity compared with some other elements (Al, P, Ca, Sc, Ti, Cr, Fe, Ga, Y, Zr and Nb). *J. Petrol.* **50**, 1765–1794.

Mallmann G. and O'Neill H. C. St. (2013) Calibration of an empirical thermometer and oxybarometer based on the Partitioning of Sc, Y and V between olivine and silicate melt. *J. Petrol.* **54**, 933–949.

Mattioli G. S. and Wood B. J. (1988) Magnetite activities across the $MgAl_2O_4$ - Fe_3O_4 spinel join, with application to thermo-

barometric estimates of upper mantle oxygen fugacity. *Contrib. Mineral. Petrol.* **98**, 148–162.

Meirer F., Cabana J., Liu Y. J., Mehta A., Andrews J. C. and Pianetta P. (2011) Three-dimensional imaging of chemical phase transformations at the nanoscale with full-field transmission X-ray microscopy. *J. Synchrotron Radiat.* **18**, 773–781.

Meirer F., Liu Y., Pouyet E., Fayard B., Cotte M., Sanchez C., Andrews J. C., Mehta A. and Sciau P. (2013) Full-field XANES analysis of Roman ceramics to estimate firing conditions - a novel probe to study hierarchical heterogeneous materials. *J. Anal. At. Spectrom.* **28**, 1870–1883.

Nimis P., Goncharov A., Ionov D. A. and McCammon C. (2015) Fe^{3+} partitioning systematics between orthopyroxene and garnet in mantle peridotite xenoliths and implications for thermobarometry of oxidized and reduced mantle rocks. *Contrib. Mineral. Petrol.* **169**, 6. https://doi.org/10.1007/s00410-014-1101-8.

O'Neill H. St. C. and Wall V. J. (987) The olivine-orthopyroxene-spinel oxygen geobarometer, the nickel precipitation curve, and the oxygen fugacity of the Earth's upper mantle. *J. Petrol.* **28**, 1169–1191.

Partzsch G. M., Lattard D. and McCammon C. (2004) Mössbauer spectroscopic determination of Fe^{3+}/Fe^{2+} in synthetic basaltic glass: a test of empirical fO_2 equations under superliquidus and subliquidus conditions. *Contrib. Mineral. Petrol.* **147**, 565–580.

Pouyet E., Fayard B., Salomé M., Taniguchi Y., Sette F. and Cotte M. (2015) Thin-sections of painting fragments: Opportunities for combined synchrotron-based micro-spectroscopic techniques. *Heritage Sci.* **3**. https://doi.org/10.1186/s40494-014-0030-1.

Prescher C., McCammon C. and Dubrovinsky L. (2012) MossA - a program for analyzing energy-domain Mössbauer spectra from conventional and synchrotron sources. *J. Appl. Crystallogr.* **45**, 329–331.

Pownceby M. I. and O'Neill H. St. C. (1994) Thermodynamic data from redox reactions at high temperatures. IV. Calibration of the Re-ReO_2 oxygen buffer from EMF and NiO+Ni-Pd redox sensor measurements. *Contrib. Mineral. Petrol.* **118**, 130–137.

Rosenthal A., Yaxley G. M., Green D. H., Hermann J., Kovács I. and Spandler C. (2014) Continuous eclogite melting and variable refertilisation in upwelling heterogeneous mantle. *Sci. Rep.* **4**, 6099. https://doi.org/10.1038/srep06099.

Schuth S., Rohrbach A., Munker C., Ballhaus C., Garbe-Schonberg D. and Qopoto C. (2004) Geochemical constraints on the petrogenesis of arc picrites and basalts, New Georgia Group, Solomon Islands. *Contrib. Mineral. Petrol.* **148**, 288–304.

Stagno V. and Frost D. J. (2010) Carbon speciation in the asthenosphere: Experimental measurements of the redox conditions at which carbonate-bearing melts coexist with graphite or diamond in peridotite assemblages. *Earth Planet. Sci. Lett.* **300**, 72–84.

Sutton S. R., Jones K. W., Gordon B., Rivers M. L., Bajt S. and Smith J. V. (1993) Reduced chromium in olivine grains from lunar basalt 15555: X-ray absorption near edge structure (XANES). *Geochim. Cosmochim. Acta* **57**, 461–468.

Toplis M. J. (2005) The thermodynamics of iron and magnesium partitioning between olivine and liquid: Criteria for assessing and predicting equilibrium in natural and experimental systems. *Contrib. Mineral. Petrol.* **149**, 22–39.

Vader V. T., Pandav R. S. and Delekar S. D. (2013) Structural and electrical studies on sol–gel synthesized fine particles of Mg–Ni ferrichromite. *J. Mater. Sci.-Mater. El.* **24**, 4085–4091.

Wilke M., Farges F., Petit P.-E., Brown, Jr., G. E. and Martin F. (2001) Oxidation state and coordination of Fe in minerals: An Fe K-XANES spectroscopic study. *Am. Mineral.* **86**, 714–730.

Wilke M., Partzsch G. M., Bernhardt R. and Lattard D. (2005) Determination of the iron oxidation state in basaltic glasses using XANES at the *K*-edge. *Chem. Geol.* **220**, 143–161.

Wong J., Lytle F. W., Messmer R. P. and Maylotte D. H. (1984) *K*-edge absorption spectra of selected vanadium compounds. *Phys. Rev. B* **30**, 5596–5609.

Woodland A. B. and O'Neill H. St. C. (1997) Thermodynamic data for Fe-bearing phases obtained using noble metal alloys as redox sensors. *Geochim. Cosmochim. Acta* **61**, 4359–4366.

Woodland A. B., Kornprobst J. and Tabit A. (2006) Ferric iron in orogenic lherzolite massifs and controls of oxygen fugacity in the upper mantle. *Lithos* **89**, 222–241.

Wood B. J. and Virgo D. (1989) Upper mantle oxidation state: ferric iron contents of lherzolitespinels by ^{57}Fe Mössbauer spectroscopy and resultant oxygen fugacities. *Geochim. Cosmochim. Acta* **53**, 1227–1291.

Associate editor: Michael J Toplis